JOURNAL OF MECHANICAL ENGINEERING AND SCIENCES
ISSN: 2289-4659 e-ISSN: 2231-8380
VOLUME 19, ISSUE 4, 2025, 10923 - 10952
DOI: https://doi.org/10.15282/jmes.19.4.2025.8.0856

RESEARCH ARTICLE

Statistical analysis of the influence of geometric parameters on static crack growth

Dheeraj Gunwant

Department of Mechanical Engineering, Apex Institute of Technology, Rampur 244921, Uttar Pradesh, India

ABSTRACT - This study integrates advanced statistical techniques with Linear Elastic Fracture Mechanics (LEFM) to assess geometric parameter contributions to crack behaviour in a stepped bar. The component was subjected to static flexural loading (600 kN) using ANSYS Workbench, where Stress Intensity Factor (SIF) and crack extension were determined via Separating Morphing and Adaptive Re-meshing Technology (SMART). Twenty-seven Central Composite Design (CCD) experiments evaluated the influence of minor and major radii, height, fillet radius, and bore depth. Regression and ANOVA analyses identified height as the most significant factor affecting crack extension. Response Surface Methodology (RSM) contour plots demonstrated that higher height, combined with low fillet radius and bore depth, resulted in SIF values exceeding 2200 MPa√mm. The developed models explained up to 99.07% of the variability. These findings provide guidelines for geometry optimisation to enhance the fracture resistance of stepped components in critical load-bearing applications.

ARTICLE HISTORY
Received : 26th Jan. 2025
Revised : 22nd Oct. 2025
Accepted : 22nd Oct. 2025
Published : 29th Dec. 2025

KEYWORDS
Linear elastic fracture mechanics
Design of experiments
Response surface methodology
Finite element analysis
Central composite design

1. INTRODUCTION

In August 2007, the Mississippi River bridge (I-35W) collapsed catastrophically, resulting in the untimely death of 13 individuals and injuring more than 100. The sudden collapse of the bridge was later attributed to the critical failure of the connecting gusset plate under the weight of traffic during rush hour [1, 2]. Fracture mechanics is used to determine the failure probability of a cracked structure under static and dynamic loading conditions. Linear elastic fracture mechanics (LEFM) is extensively employed to investigate the effect of cracks and notches on a structure's integrity. The stress intensity factor (SIF) is a single parameter generally used to represent the stresses at the crack tip. It can be used to quantitatively examine the fracture strength of a structure with inherent defects. The determination of SIF has evolved over the last several decades.

In 1957, Irwin formulated analytical solutions for calculating SIF in idealised geometries using LEFM [3]. In 1968, Rice introduced the concept of path-independent J-integral, augmenting the theoretical analysis capability for non-linear materials [4]. The development of experimental techniques led to the emergence of photoelasticity and caustics, offering novel insights into the crack fields in complex structures [5]. The Finite Element Method (FEM) transformed the numerical determination of SIF with contour integral and virtual crack closure technique (VCCT) approaches [6]. The conventional FEM struggled with mesh dependence near the crack tip, leading to the emergence of mesh-free (Galerkin) and extended finite element method (XFEM) approaches in the 1990s and 2000s. These techniques decouple the crack growth from the mesh topology, eventually alleviating such issues. The XFEM approach rests on the premise that a non-conforming mesh with a modified displacement interpolant considers boundary features [7]. It is computationally efficient for simpler geometries, but struggles with complex 3D geometries. The boundary element method also emerged for the accurate determination of SIF in infinite domains.

However, this technique has its limitations regarding dynamic re-meshing and nonlinearity [8]. The adaptive mesh refinement techniques that have emerged over the past few decades have demonstrated high accuracy with relatively low computational resource utilisation. This technique is fit for the fatigue and phase-field fracture models [9]. Surrogate models have been applied to predict the SIF in cracked offshore piping [10]. The initial model was developed using 1-D edge crack growth and subsequently extended to a 2-D growth problem in the pipe wall. The SIF for various crack lengths and depths was calculated through FEM. The implementation of machine learning techniques makes the procedure rapid, accurate, and computationally efficient compared to the traditional FEM. Numerous other analytical and numerical techniques have also been proposed to estimate the SIF. The singular integral equation method models the crack geometry but depends upon the discretisation [11]. The integral transforms yield satisfactory results in elastic media for ideal boundary conditions, but are less accurate for realistic boundary conditions [12]. The Laurent series expansion exhibits high accuracy near the crack tip but struggles in cases of complex geometries [13]. The discrete element methods suffer from parameter sensitivity issues and high computational intensity [14].

Numerical simulation-based crack-growth analysis relies on empirical techniques that require extensive calibration to obtain accurate solutions [15, 16]. The Green's function method [17] and conformal mapping [18] are highly efficient for simpler geometries but lack accuracy and generality for heterogeneous domains. The phase-field methods and cohesive zone modelling approach can handle the crack growth more accurately but suffer from high computational resource requirements [19, 20]. In these techniques, the obtained value of the SIF is compared with the material's fracture

*CORRESPONDING AUTHOR | D. Gunwant | ✉ mailto.dheerajgunwant@gmail.com

toughness to comment on its fracture resistance under static or fatigue loading [21, 22]. Precise computational methods are thus desirable for predicting crack propagation under static and dynamic loading scenarios [23]. FEM has been reported as a crucial technique for computing the SIF by [24]. Augmented visualisation through animations, colour maps, and contours in FEM helps understand structural behaviour under diverse conditions [25]. An in-depth review of the advancements in experimental, theoretical, and numerical techniques in the field of multicrack fracture mechanics has been reported [26]. These authors have highlighted the visualisation capabilities of FEM in the case of multiple interacting cracks. The analytical techniques fail to capture these insights accurately. Conversely, the FEM visualisations facilitate researchers' better understanding of crack coalescence behaviour, enabling them to make more informed decisions.

The FEM relies on mesh refinement near discontinuities to accurately capture crack growth. However, the mesh refinement must be balanced with the element quality to obtain optimal solution accuracy. Convergence is typically achieved in fracture mechanics problems when changes in the response variables, such as the SIF, fall below 1-2% [27]. Other parameters, such as energy release rates and averaged values, must be employed for convergence testing near the crack tip due to the singularity [28]. However, excessive mesh refinement (aspect ratio > 5 or Jacobian determinants < 0.6) can lead to a drastic reduction in solution accuracy due to element distortion [28, 29]. This anomaly results from interpolation errors, an ill-conditioned stiffness matrix, and solver instability. Such stringent conditions demand adaptive mesh refinement that targets the crack tips in fracture mechanics simulations. Several types of finite elements have been employed to represent cracks in a given structure and obtain accurate results. In the past, hexahedral meshes have been used extensively for regions near cracks [30]. However, the high effectiveness of the tetrahedral mesh in capturing stress-field singularities makes it optimal for most simulations [31, 32]. Notably, real-world structures, such as pipelines, pressure vessels, and turbine blades, undergo mixed-mode loading; however, most crack growth studies focus on mode-I cracks [33].

Gope *et al.* reported an increase in the SIFs with crack offset distance in the case of interacting offset and collinear cracks in a rectangular plate [25]. Crack offset distance, von Mises stress, and SIFs were analyzed using the one-factor-at-a-time approach while controlling for applied load, crack length, and specimen geometry. The Design of Experiments (DoE) approach can be a more effective option in such situations, allowing for the simultaneous evaluation of the influence of multiple factors and facilitating a deeper understanding of the interactions. The number of experiments can be effectively reduced by employing this technique. Theoretical and experimental approaches provide valuable insights into fracture behaviour; however, their simple assumptions limit their applicability to idealised boundary conditions and geometries. Contrarily, real-world problems with complex geometry and boundary conditions, material nonlinearities, and heterogeneities necessitate numerical approaches such as FEM for accurate analysis.

Subbaiah & Bollineni determined the SIF of inclined edge cracks present on the inner surface of a cylindrical pressure vessel via a 2D axisymmetric FE model [34]. These authors highlighted the relative dominance of Mode II loading as the crack inclination increases beyond 30°. As the inter-crack spacing increases beyond a point, the mode I and mode II ratios become constant due to negligible interaction between the stress fields. A FEM-based approach for SIF determination near the crack tip has been proposed [35]. These authors employed tetrahedral finite elements for meshing with a circular ring-shaped mesh near the crack tip. The hexahedral elements require a structured mesh and undergo distortion near the curved crack fronts. Conversely, a tetrahedral mesh enables localised refinement, accurately capturing the crack field stresses by conforming to the complex geometry. Their flexibility in unstructured meshing renders them ideal for adaptive mesh refinement methods [36]. For smaller cracks, FEM underestimated the normal stresses but overestimated them for larger cracks. A 2D FEM model has been presented for determining SIF in a rectangular plate with an inclined crack under biaxial loading [37]. They used analytical equations for a central inclined crack under biaxial loading to validate the results obtained from the FEM. The deviation of less than 0.5% showed excellent agreement between the analytical and numerical approaches. The magnitude of K_I increased for a single crack with the inclination angle. In the case of multiple cracks, the magnitude decreased for inclination angles of 28º to 32º. The influence of the interaction between the stress fields of different cracks diminished KI as the inter-crack spacing increased.

Bisht *et al.* have observed the shielding and intensification effects of multiple cracks on a rectangular plate subjected to uniaxial loading conditions [24]. Neighboring cracks enhance K_{II}, which is otherwise absent in the single-edge crack under uniaxial loading. It was concluded that the neighboring cracks posed a danger to the structural integrity. Increasing the crack offset distance increases the von Mises stress near the crack tip. Shearing stress decreased with increased crack offset distance, indicating that K_{II} mainly occurs due to the shear component. The shielding effect on K_I was observed due to neighboring cracks, which was exacerbated by reducing the inter-crack spacing. Multi-crack fracture mechanics is a vital field focused on the initiation, propagation, and interaction of cracks in ductile and brittle materials. Wang *et al.* have reviewed the methodological advancements in the experiments, theory, and numerical modelling of cracks [26]. While experimental results provide valuable insights into fracture behaviour, they are hindered by poor repeatability and high setup costs. Theoretical techniques are primarily limited to idealised, simple geometries and lose accuracy as repeatability increases. Numerical methods have emerged as powerful tools for simulating complex crack behaviour, but they suffer from high computational costs and stability issues. Future studies should focus on enhancing the experiments, developing models for complex shapes, and improving computational efficiency.

The traditional one-factor-at-a-time approach becomes inconsequential in the case of fracture mechanics due to its inability to capture interaction effects. This limitation is exacerbated by strong interaction effects resulting from the

involvement of multiple factors, including mixed-model loading, variable crack lengths, and complex geometry. These factors significantly influence the SIF and crack propagation. The DoE approach mitigates these drawbacks by allowing simultaneous variation in multiple fracture parameters, capturing both main and interaction effects accurately [38]. Pelegri and Tekkam studied the maximisation of mode I critical delamination fracture toughness (G_{IC}) of graphite/epoxy composite laminates using Taguchi arrays and DoE [39]. These researchers studied the main and interaction effects on G_{IC} by considering both continuous and discrete factors simultaneously, using a fractional factorial design. The response equations were developed by considering various factors, including stacking angle, stacking sequence, thickness, length, and width. A specialised subset of DOE, Response Surface Methodology (RSM) focuses on obtaining optimal responses under the influence of various input variables. The DOE identified statistically significant factors by systematically exploring the experimental domain. Once the critical variables are established, the RSM utilises a second-order polynomial to optimise the response within the specified region. This approach yields a robust two-step method, consisting of factor screening followed by optimisation within the given space. In fracture mechanics, DOE may be employed to identify key parameters that influence crack behaviour, such as load intensity, crack length, and material properties. Once identified, the RSM may be utilised to develop predictive models for minimizing the crack propagation or stress intensity. RSM uses statistical methods to model both independent and dependent variables via a second-degree polynomial function [40]. De Assis & Gomes employed artificial neural networks, metaheuristics, and RSM to solve the crack identification problem in a thin rectangular plate [41]. Using these techniques, they were able to correctly identify the crack extension, location, and orientation with errors < 1%.

These statistical techniques can be employed to investigate fracture parameters and crack propagation in defective structures with varying geometric features. Recent studies have integrated machine learning, DoE, and RSM to model fracture parameters effectively. These methods can reduce the computational cost by estimating the numerical outputs using high-fidelity data [10]. Table 1 summarises the geometries studied, methods used, and key findings of the leading publications on crack analysis.

Table 1. Summary of geometries studied, methods used, and key findings

S. No.	Geometries Studied	Methods Used	Key Findings	Authors
1	Cracked offshore piping	Surrogate modelling with FEM data	Initial model was developed as a 1-D edge crack growth and subsequently extended to a 2-D growth problem in the pipe wall	[10]
2	General crack geometries	Singular Integral Equation	Captures crack shape; accuracy depends on discretisation	[11]
3	Elastic media	Integral Transforms	Good for ideal BCs; less accurate for realistic BCs	[12]
4	Near the crack tip	Laurent Series Expansion	High tip accuracy; poor with complex geometries	[13]
5	General domains	Discrete Element Method	Sensitive to parameters; computationally intensive	[14]
6	Crack growth simulation	Numerical methods	Empirical; needs heavy calibration	[15, 16]
7	Multiple cracks in the plate	FEM	Observed K_I, K_{II} changes due to crack interaction	[24]
8	Internal axial cracks in cylindrical pressure vessels	2D axisymmetric FE model	Relative dominance of mode II loading beyond 30º crack inclination Mode I and mode II ratios become constant as the inter-crack spacing increases	[34]
9	Curved crack fronts	FEM with tetra mesh	Tetra mesh better captures complex fields	[35]
10	Inclined cracks in plates	2D FEM + Analytical	Deviation <0.5% confirms FEM validity	[37]

Based on these studies, this study uses Separating Morphing and Adaptive Re-meshing Technology (SMART), an adaptive mesh refinement-based method with advanced statistical analysis, to determine SIF and crack extension. SMART separates the crack tip geometry dynamically from the mesh, allowing the mesh to morph and conform to the evolving crack front while localizing mesh refinement. By combining advanced statistics with the SMART technique, this investigation aims to bridge the literature gap, achieving scalability to complex geometries and loading scenarios.

In this paper, we investigate the impact of the geometry of a cracked stepped bar on specific response parameters. The SMART methodology available with ANSYS Workbench (ANSYS WB) was used to determine the SIF and crack extension under predetermined loading conditions. Five geometrical parameters were considered input parameters, and SIF and crack extension were selected as response parameters. A Central Composite Design (CCD)-based DoE array was developed using ANSYS WB, and twenty-seven numerical experiments were performed using FEM to obtain the responses. Regression modelling and ANOVA were performed using Minitab, and insightful conclusions were drawn

from main and interaction effects, as well as Pareto charts and standardised impact charts. RSM was employed to develop contour plots to understand the effects of various input parameters on the response parameters.

2. DOE AND RSM

As explained earlier, the conventional one-factor-at-a-time approach has limited applications in fracture mechanics. This limit stems from the failure to capture the interaction effects between the key fracture parameters. In fracture mechanics, parameters such as fillet radius, crack length, and specimen geometry interact nonlinearly with each other, significantly influencing the SIF and crack propagation. For example, variation in crack length may indicate one trend, but altering the geometric constraints may change the actual response remarkably. The conventional one-factor-at-a-time approach misses such interactions, but the DoE technique effectively captures them. DoE allows the simultaneous variation of multiple input parameters, enabling the determination of both main and interaction effects.

The main strength of DoE lies in identifying interactions between the input variables and the response variable by varying multiple factors simultaneously. Using full or fractional factorial designs, the experimenter can simultaneously examine all possible or partial factors [42]. A full factorial design requires experiments with all possible combinations of factor levels to extract the maximum amount of information. Conversely, the fractional factorial design requires fewer parameters and computational resources. The sensitivity of each factor can be determined individually or in combination with other factors. In this manner, a causal predictive model can be established through DoE due to the independence of the input factors from one another. Factorial designs are crucial components of DoE for understanding the effects of multiple factors, including loading, material type, crack length, and orientation, on SIF and crack propagation. In a full factorial design, all possible combinations of factor levels are tested, making the total number of experiments equal to L^k. Where 'L' is the number of levels per factor and 'k' represents the number of factors. This approach captures both main and interaction effects, but becomes impractical with a higher number of factors due to the exponential increase in the number of experiments required. Contrarily, the fractional factorial designs utilise only a strategically selected subset of combinations $\left({}^{1}/_{2} \times L^{k}\right)$, effectively reducing the experiment runs. The trade-off is struck by neglecting higher-order interaction terms and capturing the most influential ones. This trade-off is particularly beneficial in fracture mechanics, where computational and experimental costs are relatively high, and the interaction between the factors is critical. Thus, fractional factorial designs are highly efficient and practical for fracture mechanics problems.

The DoE commences with screening experiments to identify consequential factors via full or fractional factorial designs, followed by refinement using RSM. Generally, the response variable is continuous and smooth, such as purity, weight, cost, and yield, but it is an unknown function of the independent variables. Conversely, the input variables, such as pressure, temperature, and velocity, possess actual values and can be controlled accurately. When plotted against the independent variable combinations, the average response develops a smooth surface called the 'response surface'. Developing the response surface allows the designer to obtain a feasible combination of the independent variables, maximizing (or minimizing) the response. While DoE is used to identify the region of interest within the factor space, RSM thoroughly explores this region by fitting a polynomial surface to it.

The mathematical model (polynomial equation) describing the response surface is fitted to the experimental data. Equation 1 represents a general second-order polynomial [43].

$$y = \beta_0 + \sum_{i=1}^{k} \beta_i x_i + \sum_{i=1}^{k} \beta_{ii} x_i^2 + \sum_{i=1}^{k-1} \sum_{j=i+1}^{k} \beta_{ij} x_i x_j \quad (1)$$

where,

Y = Response variable such as SIF, J-integral, or crack growth rate.

β_0 = Intercept term, depicting the mean response when all the input variables are at their baseline.

$\beta_i X_i$ = Linear function representing the effect of each input factor, such as load amplitude, material toughness, or crack length

$\beta_{ii} X_i^2$ = Quadratic term for accounting for the non-linear effects w.r.t. input variables.

$a_{ij} X_i X_j$ = Interaction terms depicting the combined effect of two variables, such as crack length and load, on the response variables.

This model is instrumental in understanding the influence of multiple input variables on crack behaviour in fracture mechanics. However, the second-order models suffer from the limitation of assuming continuous and smooth behaviour, which may fail in capturing the rapid transitions in fracture problems. These models are accurate within a localised region; extrapolation beyond this region may result in a loss of accuracy. Most real-world fracture problems may involve path dependency, higher-order nonlinearities, and discontinuities that second-order models may not capture. In fracture mechanics, the SIF, crack growth rate, and J-integral are generally considered typical response variables. These parameters are crucial in quantifying the crack-propagation factors of a material's fracture resistance. The selection of proper response variables is critical in establishing robust targets for RSM-based optimisation once the screening of factors is complete. A probability-based fatigue integrity evaluation was conducted to analyze the uncertainty in crack

growth due to initial flaws and material variability using DoE and RSM [44]. The DoE was employed to locate multiple points on the response surface to obtain critical accuracy. A second-order polynomial was constructed using RSM for the life cycle estimation of cracked specimens. The RSM model predicted 9,900 to 27,680 cycles to failure for a crack length of 10 mm, with an R^2 value of 0.994, demonstrating high accuracy. Several studies have shown the effectiveness of RSM in optimizing complex mechanical problems under coupled loading scenarios and environments. For example, RSM has been effectively employed to optimise the recycled concrete aggregates and cement content in cement-treated recycled concrete aggregate samples with various cement concentrations [45]. The study highlights the utilisation of demolition waste for road construction by partially (or entirely replacing the natural aggregates. The results display up to 70% replacement of natural aggregates, meeting the Indian Road Congress specifications. This result highlights RSM's capability to predict non-linear interactions involving multiple factors. Such a requirement is essential in fracture mechanics problems where crack propagation is affected by the geometry parameters and loading conditions. Similarly, the analysis of fatigue damage in deepwater risers using RSM revealed the influence of wall thickness, S-N curves, and drag in robust damage predictions [46].

These authors were able to significantly reduce the number of simulations while simultaneously improving the reliability of the results. The present study also employs this advantage by implementing RSM to reduce the number of FE simulations. This advantage is achieved without compromising the model's accuracy in capturing the key geometrical factors related to the SIF and crack extension. Additionally, the successful combination of DoE and RSM in fatigue, corrosion, and fiber concentration on the pavement concrete [47]. The use of CCD-based DoE for identification of testing levels and RSM for response analysis has been presented. The RSM could determine optimal fiber concentration for enhancing the fatigue and corrosion resistance in pavement concrete. This finding supports our use of CCD-based DoE and RSM for developing complex behaviour associated with fracture problems. Together, these precedents provide strong justification for the methodology used in the present analysis, confirming the adaptability of RSM to fracture mechanics problems. DoE and RSM are robust statistical techniques that extensively investigate and optimise the response variable with respect to the input variables. However, the potential of these techniques in LEFM and crack growth analysis has been given less attention. CCD is a statistical method for creating a continuous variable surface model to analyze factor interactions, resulting in less experimentation, shorter design cycles, and higher accuracy [48]. It is well-suited for sequential experimentation, facilitating substantial information and avoiding a lack of fit even with fewer experiments. It is particularly appropriate for investigating factors with 3-5 levels. Figure 1 shows three types of points: factorial points, a central point, and axial points located at a distance (α) from the central point. It consists of an embedded factorial (or fractional factorial design) with a centre point, supplemented with axial points, which allows for the approximation of curvature. The axial points represent novel extreme values of each design factor.

CCD was employed to model and optimise the bulk density and compressive strength of metakaolin-based geopolymers using four synthesis parameters [49]. RSM surface plots and ANOVA were used to determine the optimum conditions for geopolymer formation. The curing temperature did not affect the bulk density; however, the compressive strength decreased with increasing temperature. The highest desirability was observed for the curing temperature (67°C), followed by $SiO_2/Al2O_3$ (2.90), Na_2O/Si_2O (0.20), and H_2O/Na_2O (13.75) molar ratios. At this point, the optimum bulk density and compressive strength were 1.55 g/cc and 64.1 MPa, respectively. The optimisation of geological polymers using RSM and CCD has been reported [50]. Four critical parameters —curing temperature and time, Na_2SiO_3 content, and the fly ash-to-slag ratio —were identified for the study. The effect of these parameters on the bending strength was determined, and the significant factors were identified through regression analysis and ANOVA. The optimum parameters were calculated as NaOH and Na_2SiO_3 contents of 3% and 19.52%, respectively, with curing times of 3, 2.25, and 2.32 hours at temperatures of 80, 120, and 250°C, respectively. RSM-based calculations of thermal comfort enhancement and energy savings in buildings have been reported using a single-family house model situated in various climatic conditions [51]. These researchers highlighted the suitability of a simplified model for analyzing the building's energy performance. With a negligible 3% deviation from the software-based solution, the simplified RSM-based models can significantly reduce costs, computational time, and human resources. The experimental runs in a typical CCD analysis can be expressed by Equation 2 [52].

$$N = 2^{\mathrm{k}} + 2k + c_{\mathrm{p}} \tag{2}$$

here, 'k' and 'c_p' represent the central point's independent variables and the replicate number. The distance between central and axial points 'α' can be calculated using Equation 3 with only quintuplet levels applied [53].

$$\alpha = 2^{(k-p)/4} \tag{3}$$

For a face-centred design, α=1, implying that the design space is a cube with only three levels. The number of experiments is highest in the case of the full-factorial design, followed by the CCD and Box-Behnken designs, respectively. Figure 1 illustrates the graphical representation of a CCD, showing its various components.

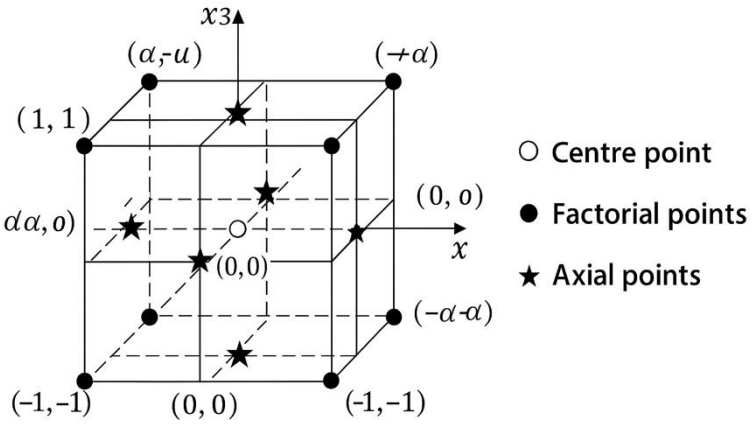

Figure 1. Graphical representation of CCD showing centre, factorial, and axial (or star) points. In fracture mechanics, these points illustrate various levels of input variables, facilitating the determination of SIF and crack growth rate through RSM

The factorial points (●) are located at the corners of the cube, depicting the combination of high and low levels of each factor. The axial points (★) are located along each axis at a distance of ±α from the centre for curvature estimation. These allow the approximation of quadratic effects. Finally, the centre points (○) are located at the midpoint of all factors and are employed to calculate the experimental errors. The key input variables, including the major and minor radii of the semi-elliptical crack and the fillet radius, were used as input parameters. The response variables, viz., SIF and crack extension, were measured at each design point to create the response surface model. The model was subsequently used to predict variations in the response variable w.r.t. input variables.

3. RESEARCH RATIONALE, GAPS, AND METHODOLOGICAL FRAMEWORK

Despite tremendous advancements in fracture mechanics, several studies still rely on a simplified crack geometry and a one-factor-at-a-time approach for analysis. This approach fails to capture the interaction effects among various input parameters, such as fillet radius, major and minor semi-elliptical radii, bore depth, and height. The limitations of conventional crack modelling approaches due to the complex loading scenario have been highlighted by [26]. Traditional modelling approaches employ either the one-factor-at-a-time or the full factorial designs, making them computationally prohibitive. The present study focuses on determining the influence of five geometric parameters on two response variables: SIF and crack extension. The SIF and crack extension in a cracked stepped bar under flexural loading are determined using the SMART module available in ANSYS WB. Statistical techniques such as ANOVA, regression, DoE, and RSM are employed to determine the quadratic and interaction effects in the FE model. Most existing studies do not integrate statistical tools such as DOE and RSM with an automated framework within the ANSYS WB environment. The combination of these two methodologies is crucial for understanding the curvature and interaction effects in fracture mechanics problems involving multiple input and response variables. Although RSM has been applied to diverse fields of engineering, its applications to the field of fracture mechanics are underutilised. The integration of Minitab-based DoE and ANSYS WB in the present study leverages SMART-based crack propagation simulations, addressing this literature gap. The objectives of the present investigation include:

- Quantitative evaluation of the individual and interactive influence of main geometric parameters, such as major and minor radii, height, fillet radius, and bore depth on the crack extension and SIF in a cracked stepped bar under static flexural loading.
- Development of predictive regression models using DoE, RSM integrated with the SMART fracture simulation tool in ANSYS WB.

  Identification of the most prominent statistically significant parameters affecting the crack growth behaviour.

4. MATERIALS AND METHODS

This section explores the methodology used to investigate the impact of geometric parameters on various response parameters. The SMART methodology, material properties, initial geometry, and input and response parameters have been presented.

4.1 Separating Morphing and Adaptive Re-Meshing Technology

Traditional numerical crack growth analysis is computationally inefficient due to the use of a hexahedral mesh for modelling the crack front. ANSYS uses the unstructured mesh method (UMM) to generate a tetrahedral mesh around the crack front [54]. UMM features an irregular grid arrangement of arbitrary shape and size, offering flexibility and enabling the modelling of curved surfaces. It allows accurate solutions near sharp gradients by eliminating the development of new elements and leveraging conventional aspects. A smaller number of discretisation nodes results in a drastic reduction in

the computational cost with a negligible drop in accuracy. Each iteration is followed by remeshing around the crack tip, focusing the computational power where it is needed the most. This strategy accelerates simulation rendering, making it scalable for larger projects. Intricate geometries can be effectively modeled by generating a tetrahedral mesh, drastically reducing mesh generation time. The accelerated speed, coupled with high precision, ensures the accurate calculation of fracture parameters [55]. A conventional hexahedral mesh may take between 48 and 168 hours. Conversely, UMM completes the mesh setup within just 10 minutes. Interestingly, SMART-based UMM with second-order tetrahedra and adaptive mesh refinement can improve the accuracy of SIF predictions by 1-3% compared to conventional results [56, 57]. The UMM creates a completely structured tetrahedral mesh using Gaussian quadrature-based 10-node second-order finite elements (SOLID187) within the given domain. The second-order mesh supersedes the linear mesh by enhancing the accuracy of stress determination near the crack fronts. It typically utilises 4-5 integration points for each tetrahedron, ensuring accurate stress-strain computation. This technique enables the calculation of fracture parameters, such as SIF and crack extension, with high integrity. Instead of creating explicit singular elements, UMM warps the tetrahedra, forcing the nodes to converge towards the crack front, effectively approximating the singular stress fields [58]. In the present investigation, the implementation of UMM resulted in a reduction of approximately 21% in total node counts. The decrease in node count resulted in an approximately 18% reduction in computational time compared to a structured mesh, with similar accuracy near the crack front. This gain in computational efficiency results from the localised refinement of the mesh near the crack front. The average element quality was improved by 5-6% due to the better ability of the unstructured mesh to conform to the discontinuity with relatively lesser aspect ratio distortion.

The fracture parameters, such as the J-integral and SIF, are determined via the domain integral method, which creates a contoured domain enveloping the crack front, ultimately allowing for accurate, path-independent calculations [58]. ANSYS implements the SMART for crack growth analysis. The SMART and XFEM techniques approach the crack initiation and growth through different strategies within the Finite Element Method (FEM) framework. The XFEM introduces enrichment functions within the displacement field using a partition of unity method. This technique enables the modelling of discontinuities independently of the mesh. For this purpose, standard shape functions with Heaviside or asymptotic crack tip enrichment are employed to represent singular fields and jumps, thereby eliminating the need for remeshing. Mathematically, the expression for displacement field $u(x)$ in XFEM is given by Equation 4.

$$u(x) = \sum_{\mathrm{i}} N_{\mathrm{i}}(x)\, u_{\mathrm{i}} + \sum_{\mathrm{j}} N_{\mathrm{j}}(x)\, H(x)\, a_{\mathrm{j}} + \sum_{\mathrm{k}} N_{\mathrm{k}}(x)\, F(x)\, b_{\mathrm{k}} \quad (4)$$

where, $H(x)$, $F(x)$ are enrichment functions with a_j and b_k are the additional degrees of freedom [59]. In contrast, the SMART employs a mesh conforming approach in which the crack is embedded and propagated by node duplication and remeshing. Instead of enriching the displacement function, it calculates the crack propagation criteria and reconstructs the mesh to conform to the new crack geometry. The XFEM is computationally efficient for small crack extensions. Conversely, SMART offers high accuracy for larger cracks with curved paths by preserving the mesh quality during remeshing cycles. This feature makes it a better choice for complex 3D crack growth. SMART minimises the computational time by using UMM-based automatic meshing of the critical region and fatigue growth analysis of cracks [60].

Unlike XFEM, SMART can be scaled up due to the superiority of meshing a small area near the crack rather than the entire domain. Figure 2 (a) displays the visual difference between the unstructured and structured meshes for the edge cracked plate with L/W=16/7 and W=7 and a/W=1/2. The magnified view of the crack front region is presented in Figure 2 (b). The iterative SMART framework is summarised in Figure 2 (c). The process begins with problem initialisation, which involves creating geometry, meshing, assigning material properties, and specifying boundary conditions. The initial crack is also defined in this step. A coarse mesh is generated around the cracks using the tetrahedral finite elements. In the second step, the initial static problem is solved to determine the stress-strain distribution within the domain. The key fracture parameters (SIF, J-integral, and energy release rate) governing the crack propagation are also calculated near the crack front. In the third step, an energy release rate or virtual crack closure technique-based criterion is subsequently employed to evaluate the crack growth direction. Subsequently, a suitable crack advancement direction is determined, and the SMART strategy is activated to handle the associated geometric changes. In the separating subroutine, nodes are duplicated around the existing nodes to initiate crack propagation. The morphing subroutine adjusts the surrounding mesh to accommodate crack advancement while maintaining mesh quality. Finally, the adaptive meshing subroutine allows mesh regeneration around the crack tip to maintain the solution accuracy. Each crack extension cycle is checked for convergence using the energy error threshold, force-displacement norms, or crack increment size to ensure the solution's numerical stability. Once the convergence criteria are met, the solution proceeds to the next load step. In the event of an unconverged solution, the solver adjusts the mesh size or load increments to restore system stability. The crack front is subsequently updated by varying its orientation and location, followed by the calculation of corresponding fracture parameters. The cyclic simulation proceeds till the termination conditions ($K_I < K_{IC}$ or $J < J_C$) are exceeded or unstable crack propagation is encountered.

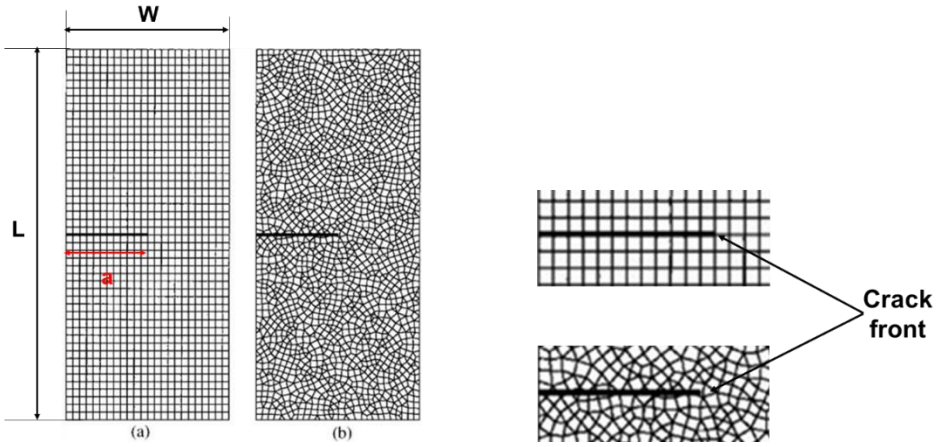

(a) (b)

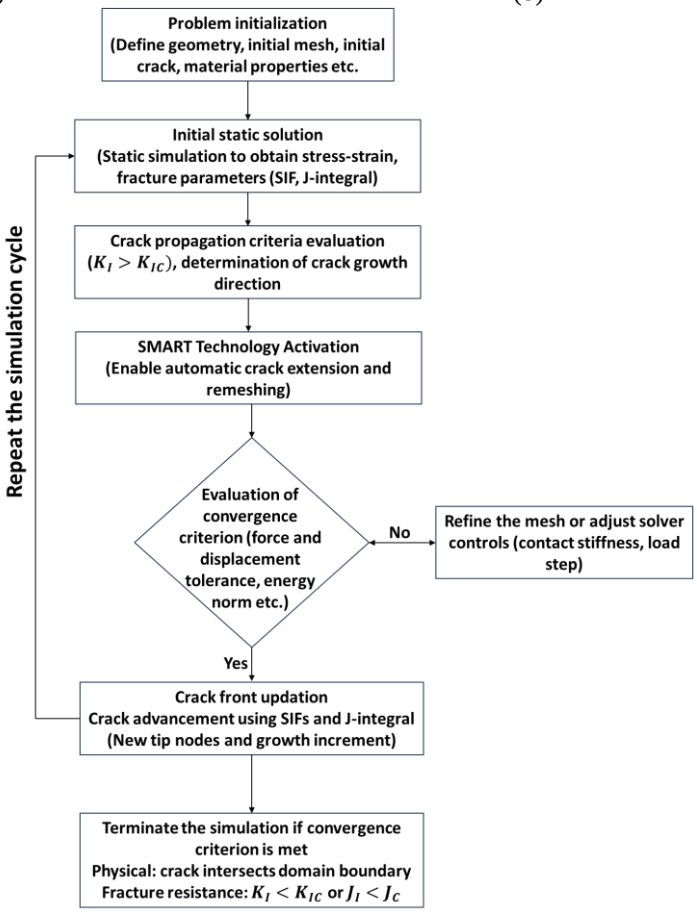

(c)

Figure 2. (a) Structured and UMM-based mesh for crack growth analysis [61], (b) Magnified view of the mesh near the crack tip, and (c) SMART framework

4.2 Geometry and Material Properties

Figure 3 illustrates the geometry of the aluminium 7075-T6 stepped bar used in the present analysis. It consists of a base with a diameter of 400 mm and a thickness of 200 mm. This base was jutted by a smaller bar of diameter 100 mm and connected via a fillet of initial radius 15 mm. The smaller diameter was hollowed up to a depth of 100 mm. A surface-breaking, semi-elliptical crack with major and minor radii of 15 and 5 mm was introduced in the bar at the fillet region. A local coordinate system with the X-axis perpendicular and the Z-axis parallel to the fillet radius was created to align the crack (highlighted in red colour). This local coordinate system results in the crack front extending into the stepped bar perpendicular to the fillet, as shown in Figures 4 (a) and (b). The stepped bar was loaded in the negative X direction. The semi-elliptical geometry is preferred over simpler shapes as it is the most common experimentally observed crack front profile. It allows accurate computation of K_I, inherently capturing the angular changes of SIF around the circumference. This geometry represents common components encountered in aerospace shafts, machinery, and pressure vessels, characterised by rotating or non-rotating members with local stress concentrators.

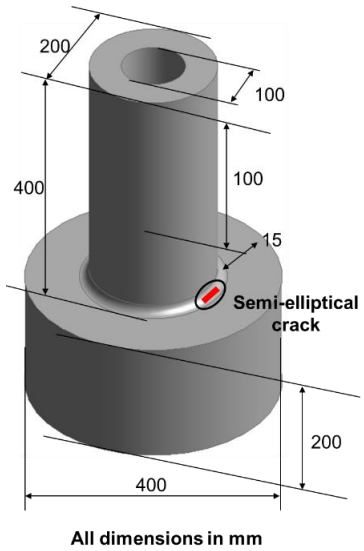

Figure 3. Geometry of the stepped bar showing all critical dimensions

As shown in Figure 4 (a), the surface-breaking crack is located on the tensile face of the stepped bar, with its orientation perpendicular to the flexural loading direction. The magnified view of the crack location is shown in Figure 4 (b). The crack geometry mimics the realistic corrosion and fatigue-induced surface defects observed in engineering components. The semi-elliptical crack shape is used to obtain an accurate prediction of the natural flaws encountered in practice. The curved crack geometry allows smooth variation of SIF along the crack front [62]. Such smooth variation is crucial for capturing the non-uniform crack advancing forces as compared to the planar cracks. The crack plane was kept perpendicular to the fillet surface by keeping the x-axis of the local coordinate system parallel to the crack front. The material properties of aluminium 7075-T6 are presented in Table 2.

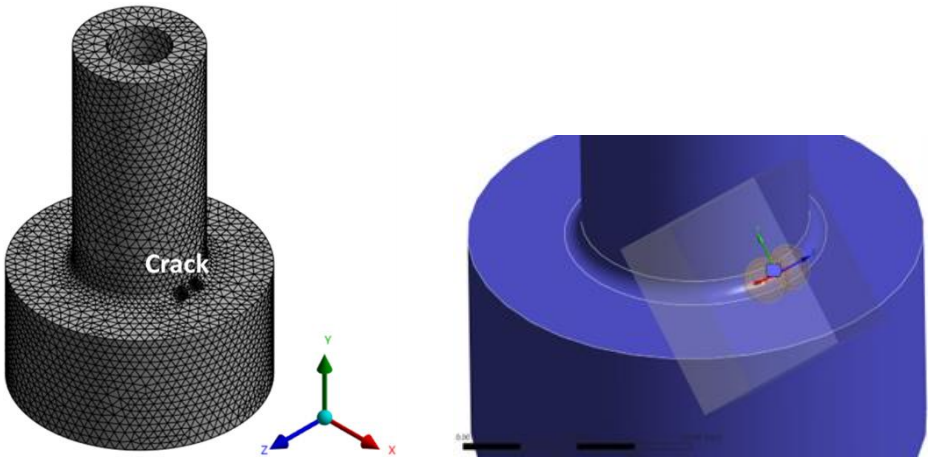

(a) (b)

Figure 4. (a) Location of the crack and coordinate system in the meshed model, and (b) zoomed view of the crack location

Table 2. Mechanical and fracture properties of aluminium 7075-T6 [63]

S. No.	Parameters	Value
1.	Young's modulus, E	71700 MPa
2.	Poisson's ratio, μ	0.33
3.	Fracture toughness, K	917.06 MPa√mm

4.3 Mesh Independence Test

In FEA parlance, mesh convergence implies obtaining the true solution of partial differential equations with a finer mesh in the spatial domain. It involves sequentially reducing the element size and analyzing the impact on the solution accuracy and computational efficiency. It is well-known that a finer mesh provides a more accurate solution due to improved sampling of the design domain. However, computational efficiency tends to decrease drastically as the element size is reduced, which necessitates the need for high-performance computing capabilities. The designers must strike the optimal balance between the solution's accuracy and computational efficiency. A mesh independence study was conducted in the present investigation to determine the optimal number of elements. Figure 5 (a)-(f) presents the results

of the mesh independence study, displaying the finer mesh with a lower element size. The maximum von Mises stress was determined for each element size, and the results are plotted in Figure 5(f). Mesh convergence was determined using the relative percentage error in the maximum von Mises stress between successive mesh refinements. The relative percentage error was calculated using Equation 5.

$$\varepsilon_{\mathrm{n}} = |(\sigma_{\mathrm{n}} - \sigma_{\mathrm{n-1}}) / \sigma_{\mathrm{n-1}}| \times 100\% \quad (5)$$

where,

σ_n = Maximum von Mises stress at the current mesh refinement

σ_{n-1} = Maximum von Mises stress from the previous mesh refinement

A tolerance convergence criterion of 1% was applied for obtaining mesh convergence. The solution was considered converged when the change in maximum von Mises stress between two successive mesh refinements was less than 1%. Figure 5 (f) illustrates the variation in maximum von Mises stress with consecutive mesh refinement levels. The relative percentage error dropped below 1% to 0.27% as the mesh was refined to approximately 49635 elements. The mesh size was further reduced, increasing the number of elements to 56362 to ensure complete mesh independence. The corresponding plateauing of the von Mises curve with the number of elements is illustrated in the Figure. The increase in computational time with the number of elements is illustrated in Figure 5 (f). The computational time increased from 22 seconds for 18653 elements to 124 seconds for a 56362-element mesh. The substantial increase in computational time is the primary reason for limiting the number of elements to 49635. This discretisation level offers the best trade-off between computational efficiency and accuracy, rendering it suitable for performing all the simulations. The convergence and reduction in simulation uncertainty with mesh refinement were demonstrated using the 95% confidence interval error bars. At each mesh size, three simulated values of von Mises stresses were determined using the normal distribution curve centred around the FE-derived value. The 95% confidence interval was subsequently calculated using Student's t-distribution and plotted as error bars (see Figure 5(f)). The narrowing of the confidence interval at higher mesh densities indicates that the mean stress is stabilised, associated with improved reliability and simulation accuracy.

4.4 Central Composite Design

CCD is a crucial statistical technique used for analyzing multifactor interactions by developing continuous variable surfaces. It results in significantly reducing design cycles with high accuracy by utilizing factors with 3-4 levels. The lack of fit is avoided, even with fewer experimental runs, ensuring substantial information is generated. The curvature effects are accurately approximated using the embedded fractional factorial design with central and axial points. The present study employs CCD using ANSYS WB to perform predetermined numerical experiments. The five input variables, major and minor radii (P9, P7), fillet radius and height (P16, P10), and bore depth were varied across the coded levels. Response variables, including crack extension and SIF, were determined for each geometry through SMART-based crack growth simulations under static flexural loading. Statistical software Minitab was used to perform the regression analysis and RSM to investigate the influence of geometric parameters on the response variables. The graphical representation of CCD has already been presented in Figure 1.

As shown in Table 3, the present investigation involves five input and two response parameters. The five input geometric parameters are depicted in Figure 6 (a)-(c). Table 4 presents the DoE array obtained using CCD and FEM. These variables were varied across three levels: low (-1), centre (0), and high (+1), resulting in a CCD array with 16 factorial points, 10 axial points, and one centre point. The axial distance 'α', representing the star point position, is calculated using Equation 6.

$$\alpha = (2^k)^{1/4} \quad (6)$$

where $'k'$ is the number of input variables (five in the present case), substituting $k = 5$, in equation 5 gives $\alpha \approx 2.0$. This value of α represents a rotatable design ensuring uniform prediction variance in all directions. However, to improve the practicability and simplify the mesh generation for axial configurations, α was set equal to 1.0. Although non-rotatable, this results in a well-spread design space for fitting second-order polynomial-based models [64]. The proposed approach allows accurate prediction of SIF and crack extension with high computational efficiency. Thereby, a total of twenty-seven numerical experiments were conducted to determine different response parameter values by varying various input parameters according to the CCD. The dataset obtained in this manner was employed to visualise the results graphically. The input parameter ranges were selected based on the combination of manufacturing, design constraints, feasibility, and previous fracture studies. The major and minor radii of the semi-elliptical crack were selected based on the surface flaws encountered in realistic machine components [62]. The stepped bar height was varied within the mentioned range to capture the influence of beam slenderness on the crack propagation under static flexural loading. The fillet radius range was typically selected based on the manufacturing tolerances for machined components and to reduce stress concentration. The bore depth represents the geometrical flaws and internal features encountered in actual structural components. In tandem, these ranges ensure the viability and feasibility of the design space, simultaneously representing the actual components.

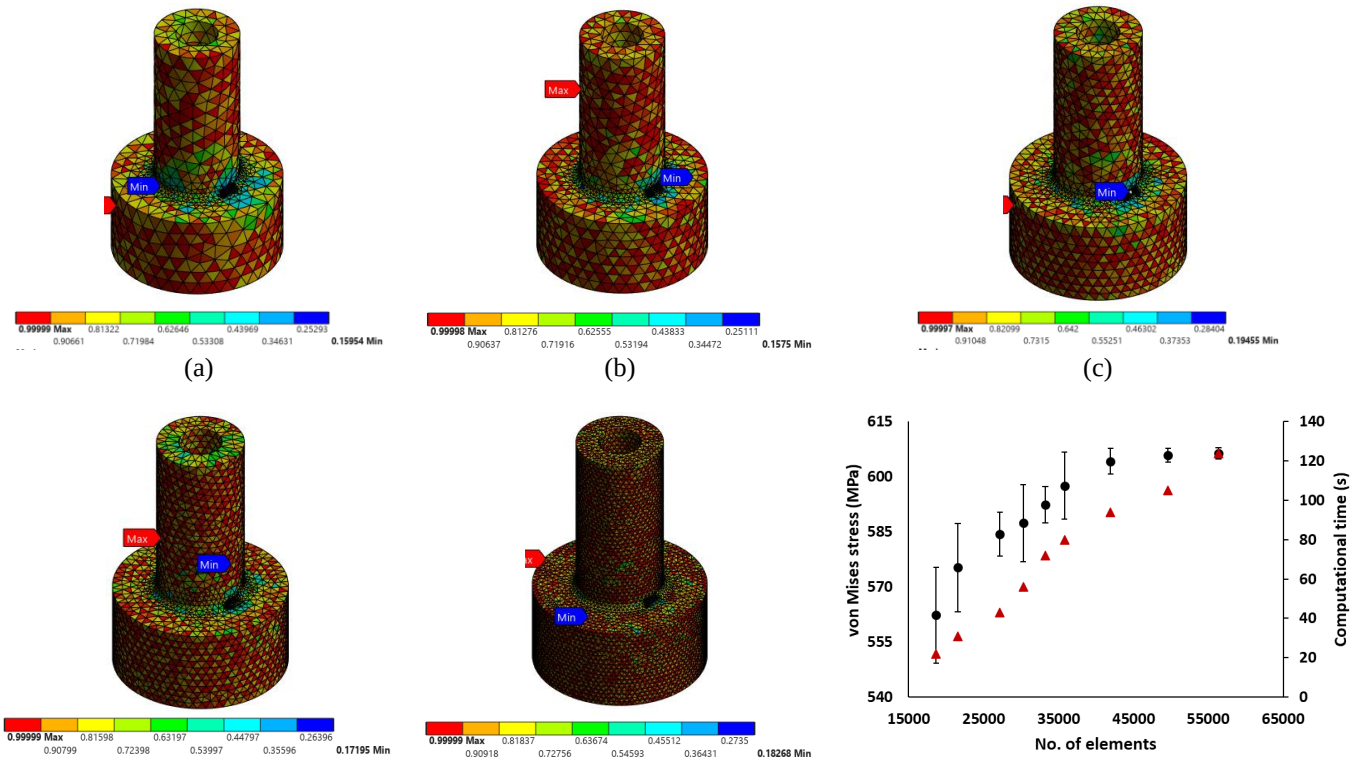

Figure 5. FE model of the stepped bar (a) 18653, (b) 30282, (c) 35787, (d) 49635, and (e) 56362 elements, (contour plots reveal the mesh metrics distribution throughout the domain), and (f) variation of von Mises stress with the number of elements

The crack extension was measured using the semi-elliptical crack's incremental growth under static flexural loading along the crack front. The crack extension values were extracted using the SMART-based crack growth module of ANSYS WB by updating the crack front position after each propagation increment. The SIF values were extracted using the energy-based J-integral method via the built-in fracture tool in ANSYS WB. This module calculates J at the predetermined crack path around the crack front. The J-integral was subsequently converted into mode-I SIF via LEFM [58].

Table 3. Input and response parameters employed in the CCD

Input parameters			
S. No.	Input parameter	Identification code	Initial value
1.	Minor radius of semi-elliptical crack (mm)	P7	5 mm
2.	Major radius of semi-elliptical crack (mm)	P9	15 mm
3.	Height (mm)	P10	400 mm
4.	Fillet radius (mm)	P16	15 mm
5.	Bore depth (mm)	P17	250 mm
Response parameters			
S. No.	Response parameter	Identification code	
1.	Crack extension (mm)	P12	
2.	Stress intensity factor (MPa.mm$^{0.5}$)	P15	

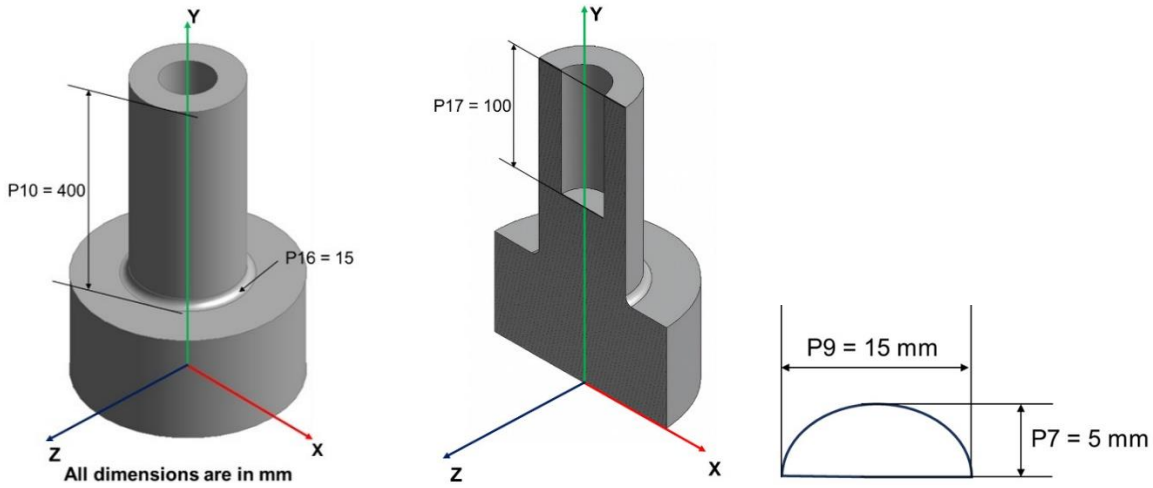

(a) (b) (c)

Figure 6. (a) CAD model of the stepped bar showing geometric parameters (Fillet radius (P16) and height (P10)) and their initial values, (b) XY cross-section of the bar showing bore depth (P17) with initial value 100, and (c) semi-elliptical crack geometry illustrating input parameters minor and major radii (P7 and P9)

Table 4. CCD DoE array with colour-coded minimum (light blue) and maximum (red) values

	Input parameters					Response parameters	
#	P7 - Semi-Elliptical Crack -- Minor Radius (mm)	P9 - Semi-Elliptical Crack --Major Radius (mm)	P10 - XYPlane.V2 (mm)	P16 - XYPlane.R6 (mm)	P17 - Extrude1.FD1 (mm)	P12 - Crack Extension Probe Crack Extension (mm)	P15 - SIF (K1) Maximum (MPa√mm)
1	5.00	15.00	400.00	15.00	250.00	23.56	1864.19
2	4.50	15.00	400.00	15.00	250.00	19.98	1794.98
3	5.50	15.00	400.00	15.00	250.00	22.98	1898.62
4	5.00	13.50	400.00	15.00	250.00	23.93	1877.88
5	5.00	16.50	400.00	15.00	250.00	23.57	1877.38
6	5.00	15.00	360.00	15.00	250.00	20.13	1638.14
7	5.00	15.00	440.00	15.00	250.00	26.08	2148.13
8	5.00	15.00	400.00	13.50	250.00	24.16	1869.93
9	5.00	15.00	400.00	16.50	250.00	21.77	1860.62
10	5.00	15.00	400.00	15.00	225.00	23.10	1883.72
11	5.00	15.00	400.00	15.00	275.00	19.40	1792.47
12	4.86	14.57	388.67	14.57	257.08	18.71	1755.66
13	5.14	14.57	388.67	14.57	242.92	18.02	1734.81
14	4.86	15.43	388.67	14.57	242.92	19.74	1768.87
15	5.14	15.43	388.67	14.57	257.08	24.66	1842.91
16	4.86	14.57	411.33	14.57	242.92	20.67	1920.85
17	5.14	14.57	411.33	14.57	257.08	22.60	1926.67
18	4.86	15.43	411.33	14.57	257.08	24.07	1945.91
19	5.14	15.43	411.33	14.57	242.92	23.80	1949.58
20	4.86	14.57	388.67	15.43	242.92	18.20	1735.34
21	5.14	14.57	388.67	15.43	257.08	18.12	1723.30
22	4.86	15.43	388.67	15.43	257.08	19.74	1760.53
23	5.14	15.43	388.67	15.43	242.92	20.16	1751.92
24	4.86	14.57	411.33	15.43	257.08	24.62	1923.22
25	5.14	14.57	411.33	15.43	242.92	22.75	1928.34
26	4.86	15.43	411.33	15.43	242.92	23.97	1943.25
27	5.14	15.43	411.33	15.43	257.08	25.49	1942.22

5. RESULTS AND DISCUSSION

5.1 Finite Element Analysis

The stress fields intensify asymptotically near the crack tip following a singularity pattern. As suggested by LEFM, the stress distribution near the crack tip is typically expressed by the equation $\sigma \propto \frac{K}{\sqrt{2\pi r}}$, where 'K' is the SIF and 'r' is the radial distance from the crack tip. This stress intensification results in an increase in the von Mises stress near the crack front and free surfaces [22]. Figure 7 (a) & (b) shows the normal and magnified von Mises stress distribution contours in the stepped bar under applied load. The highest stress, equal to 947.13 MPa, occurred at the crack tip. When compared to the yield strength of aluminium 7075-T6 (503 MPa), it is evident that the yield limit is exceeded at the crack tip, resulting in plastic deformation [63]. This finding suggests the existence of elastic-plastic conditions in the vicinity of the crack front, even though the surrounding material behaves elastically. Such localised plastic deformation is expected and is consistent with the small-scale yielding relative to the crack dimensions. This validates the implementation of SIF-based fracture mechanics for predicting the initial crack growth [22]. As shown in Figure 7 (c), the corresponding SIF contour in the crack displays significant stress intensification at these locations. The SIF contours were mapped onto path 1-2 to visualise the variation across the semi-elliptical crack front. The mode-I SIF varied between the lowest and highest values, with 1497.60 MPa√mm at the deepest point (point 1) and 1864.20 MPa√mm at the surface edges (point 2). At the free surface, the crack tip experiences an out-of-plane constraint, which promotes localised stress intensification. The plane stress condition at the surface leads to a higher value of SIF. Conversely, the mid-depth is subjected to higher stress triaxiality (a plane strain condition), leading to a smaller SIF value. The variation is consistent with the elliptical surface cracks experimentally studied by [62]. The geometric effects are further amplified in cylindrical and filleted geometries, particularly in stepped geometries, which intensify the local stress fields even more [65]. These values are significantly higher than the mode-I fracture toughness of aluminium 7075-T6, resulting in crack extension (see Table 2).

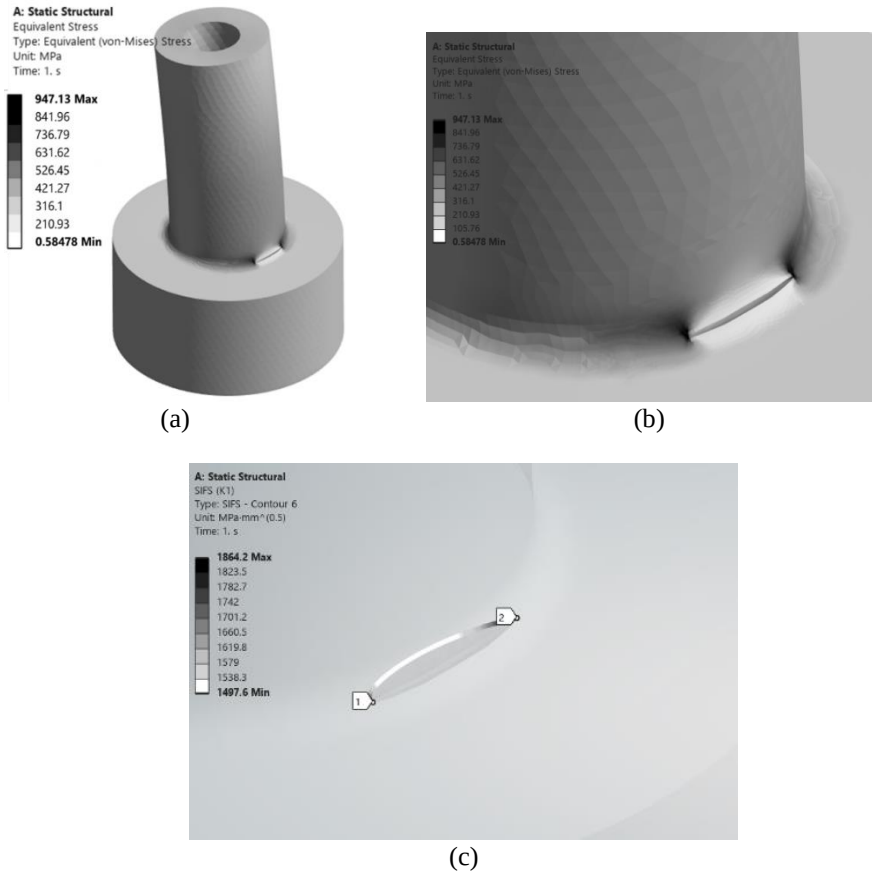

Figure 7. (a) von Mises stress distribution in the stepped bar under given loading and boundary conditions, (b) magnified view of the von Mises stress contours around the crack, and (c) SIF contour in the crack

As displayed in Figure 7 (c), the calculated maximum K_I value is 1864.20 MPa√mm at the crack surface. The K_{IC} value for aluminium 7075-T6 is 917.06 MPa√mm, resulting in a safety factor value (K_I/K_{IC}) of 0.42. A safety factor less than unity ($K_I/K_{IC} < 1$) indicates that the applied stress intensity factor exceeds the material's fracture toughness, leading to the initiation and subsequent propagation of the crack under the given loading conditions. In a physical sense, this implies an unstable fracture regime, emphasizing the need for effective crack mitigation measures to ensure structural integrity. Although a quasi-static analysis was performed, the total load was divided into a sequence of loads to enable modelling of the complex crack extension phenomenon. Figure 8 (a)-(f) shows the increase in crack extension and crack front evolution between the time steps 0.667 s and 1 s. The time steps represent the crack growth directions, and the crack

orientation is depicted through arrows and coordinate axes. The corresponding increase in crack extension over time is presented in Figure 8 (g). During the time interval 0 s to 0.6 s, there is no visible crack extension due to the elastic deformation of the material. Once the fracture toughness of the material is exceeded at 0.667 s, the crack begins to grow into the material. The crack advancement and crack extension are evident from the figure. As time progresses, the crack extension increases linearly from 3.917 mm to 23.563 mm over the time interval of 0.667 s to 1 s. A linear increase in crack extension corresponds to a stable fracture process under static loading. Figure 8 (g) depicts the variation in von Mises stress versus time under the mentioned loading conditions. During the initial loading phase between 0 and 0.6 s, a linear increase in the von Mises stress indicates the elastic material deformation. At $t \approx 0.6$ s (dashed line), the SIF reaches material's fracture toughness, marking the initiation and stable crack propagation. This finding implies that the applied load is below the critical threshold till 0.6 s and is unable to initiate the crack. Once the threshold is exceeded, a non-linear increase in the von Mises stress is noticeable from the figure. Such an effect primarily emanates from the localised plastic deformation and stress redistribution near the crack tip. After 1 s, the maximum von Mises stress and crack extension reached 947.13 MPa and 23.56 mm, respectively.

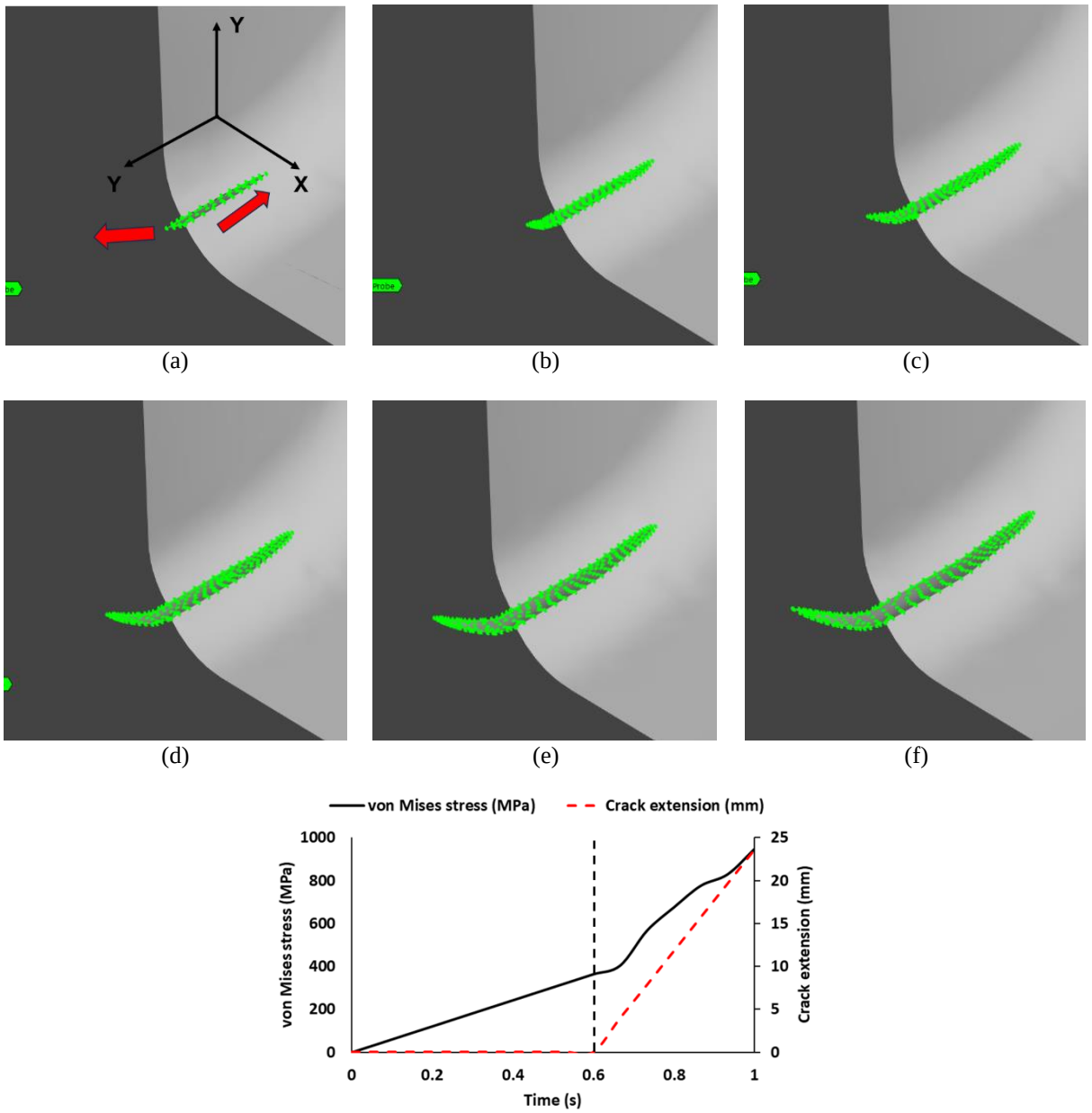

Figure 8. Crack extension at (a) 0.667 s, (b) 0.733 s, (c) 0.8 s, (d) 0.866 s, (e) 0.933 s, (f) 1 s, and (g) variation in von Mises stress and crack extension with respect to time

5.2 Statistical Analysis

5.2.1 Regression analysis and ANOVA

The regression modelling was performed using the CCD within the RSM framework. The CCD framework inherently includes linear, quadratic, and interaction terms to capture the curvature and interaction effects between various parameters. While some terms showed statistical insignificance ($p > 0.05$), they were retained to maintain the model

hierarchy and capture the possible interaction effects. A similar approach, highlighting the need for a second-order model in complex problems, has also been proposed by [40]. Hierarchy retention in RSM-based modelling ensured physical and mathematical interpretability [66]. The present investigation aims to capture the trends and interactions, rather than optimizing the model's prediction ability; the full model was retained. The regression equation for the model is presented in Equations 7 and 8. The equations are quadratic and include the individual and interaction effects of the input parameters on the response parameters.

$$\begin{aligned} P12 = {} & 183 + 297P7 - 41.7P9 - 0.42P10 - 21.8P16 - 2.95P17 - 2.19P7^2 + 0.763P9^2 + 0.00067P10^2 \\ & - 0.348P16^2 + 0.00236P17^2 - 10.06P7P9 - 0.305P7P10 + 0.43P7P16 \\ & - 0.019P7P17 + 0.07P9P10 + 0.91P9P16 + 0.113P9P17 + 0.031P10P16 \\ & + 0.00001P10P17 + 0.011P16P17 \end{aligned} \tag{7}$$

$$\begin{aligned} P15 = {} & 17325 + 3360P7 - 1407P9 - 13.9P10 - 1208P16 - 22.9P17 + 36.4P7^2 + 17.75P9^2 \\ & + 0.0346P10^2 + 0.17P16^2 + 0.0759P17^2 - 44.3P7P9 - 4.65P7P10 - 0.4P7P16 \\ & - 4.40P7P17 + 0.96P9P10 + 28.2P9P16 + 1.18P9P17 + 1.23P10P16 \\ & - 0.0672P10P17 + 1.06P16P17 \end{aligned} \tag{8}$$

Equations 7 and 8 represent the second-order polynomial regression model, which captures the influence of input variables on the response variables. The quadratic equation enables the modelling of both non-linear and interaction effects, considering the synergistic effects among multiple parameters. The quadratic model offers a trade-off between interpretability, feasibility, and accuracy within the available dataset. The three-dimensional fracture parameters often exhibit a non-linear relationship with geometric features. Moreover, the CCD employed in the present investigation is well-suited for fitting quadratic surfaces effectively, making it a reliable approach for handling fracture mechanics problems. Table 5 presents the model summary for the response surface regression model for crack extension (P12) and SIF (P15). Table 5 depicts the regression model summary. The regression model for SIF (P15) yields statistically significant results, with an R-squared value of 99.07% and an R-squared (adjusted) value of 95.97%. Accordingly, the R-sq (pred) value was 84.14%, indicating the ability of the selected parameters to explain the variability of the response variables. A low standard deviation (19.81) displays a strong predictive ability, justifying the inclusion of linear and interaction terms. The model summary for SIF (P15) indicates high statistical significance for the input variables (P7, P9, P16, P9P16, P10P16, and P7P9) with $p < 0.05$. Retaining these input variables and interaction terms renders the model interpretable and accurate. Conversely, the large discrepancy between R-sq (80.96%) and R-sq (pred) (0.00%) in the regression model for crack extension (P12) indicates poor generalisation. The R-sq (adj) value of 17.49% indicates that many of the included terms make a negligible contribution to the model accuracy. Many predictors and interaction terms, such as P10P7, P7P17, P10P17, and P16P17, display small coefficients and statistical insignificance with p-values greater than 0.1. Eliminating these terms would reduce overfitting, ultimately improving the model's parsimony without a significant loss in accuracy.

Table 5. Regression Model summary for response parameters crack extension (P12) and SIF (P15)

S	R-sq	R-sq (adj)	R-sq (pred)	Response parameter
2.090	80.96%	17.49%	0.00%	P12
19.81	99.07%	95.97%	84.14%	P15

The low R-sq (adj) and R-sq (pred) values for the crack extension response variable are duly acknowledged. These values suggest that the model is moderately fitting the data and has limited generality. However, it is emphasised that the second-order regression model was deliberately chosen, considering the nature and physics of fracture mechanics problems. As stated earlier, the CCD is highly recommended for capturing non-linear and interaction effects in problems where geometry influences the response variables. The poor statistical fit in the case of crack extension (P12) may be partially attributed to high intrinsic variability in the data. Such variability is likely due to high mesh sensitivity, numerical convergence threshold, and local mesh gradients. Similar variability in crack propagation has been reported in additively manufactured Ti-6Al-4V specimens due to the microstructural anisotropy and build orientation [67]. This observation does not necessarily invalidate the adopted methodology. Instead, it highlights the challenge associated with highly scattered fracture response variables when using regression analysis. Moreover, retaining interaction and quadratic terms is consistent with the CCD framework and comparability across the responses [64]. A reduced model may enhance model accuracy; however, it may also conceal interaction effects, thereby compromising the physical interpretation of the model. Considering this reason, we believe that the current model is sound and robust for fracture mechanics-based problems. The poor predictive performance of the model for the response variable crack extension (P12) is evident in the R-squared (adj) value of 0.00%. However, it is worth noting that the model primarily aims to investigate the influence of geometric parameters and their interaction trends, rather than high-fidelity forecasting. The lack of predictability emanates from the high numerical sensitivity and non-linear behaviour of the crack extension. Given the constraints of the current dataset and the CCD framework employed, the full model was retained to maintain consistency across responses. With the current model primarily offering qualitative insights, future work may address this limitation by using more refined modelling approaches and additional simulations.

The results of the ANOVA for the regression model of the response parameter crack extension (P12) are presented in Table 6. The 'source' column of the ANOVA lists the sources of variation, viz., factors, interactions, and error. The 'DF' column contains the independent information associated with each variation source. The total variation attributed to each source (sum of squares) and the mean square values are presented in the 'Adj SS' and 'Adj MS' columns. The 'Adj MS' column values are obtained by dividing the SS values by the DF values and representing each source's variance. The term 'Adj SS' represents the portion of the total variation in the response variable that can be attributed uniquely to the particular factor (or interaction). It takes into account the presence of other factors in the model. The contribution of the different terms in the model is adjusted to sequester the effect of the analyzed factor. The term 'Adj MS' measures the average variation in the response variable, which can be explained by the factor (or interaction) considered. The F-value represents the test statistic for comparing the variance of a factor with the variance of the error. Similarly, the P-value represents whether the factor's influence on the response variable is significant.

As evident in Table 6, a high F-value indicates that the variance explained by the factor is significantly larger than the unexplained variance in the model. The model's highest F-value for factor height (P10) was 12.48, indicating its significant effect. This finding also corroborates the Adj SS value of 54.53 for height, which is noticeably higher than all the other parameters. The P-value is 0.012, which is significantly lower than the P-values for the different variables. However, as $p > 0.05$, we fail to reject the null hypothesis (H0), implying that the variability might be due to chance. The height (P10) contributes to approximately 39.6% of the variance, rendering it the most influential geometric parameter. Other factors, such as fillet radius (10%) and minor radius (8%), are also the second and third most significant contributors. Interestingly, bore depth and most of the quadratic terms have an inconsequential contribution. This finding suggests that the model's complexity can be effectively reduced by eliminating statistically insignificant terms. Such simplification may enhance the model's parsimony without compromising its predictive capability.

Table 6. ANOVA table for response parameter crack extension (P12)

Source	DF	Adj SS	Adj MS	F-Value	P-Value	% Contribution
Model	20	111.484	5.5742	1.28	0.407	80.96
Linear	5	85.457	17.0914	3.91	0.064	62.06
Minor radius (mm)	1	11.240	11.2401	2.57	0.160	8.16
Major radius (mm)	1	5.880	5.8804	1.35	0.290	4.27
Height (mm)	1	54.525	54.5245	12.48	0.012	39.60
Fillet radius (mm)	1	13.776	13.7763	3.15	0.126	10.00
Bore depth (mm)	1	0.035	0.0355	0.01	0.931	0.03
Square	5	11.819	2.3637	0.54	0.742	8.58
Minor radius (mm)*Minor radius (mm)	1	0.382	0.3819	0.09	0.777	0.28
Major radius (mm)*Major radius (mm)	1	3.752	3.7523	0.86	0.390	2.72
Height (mm)*Height (mm)	1	1.470	1.4700	0.34	0.583	1.07
Fillet radius (mm)*Fillet radius (mm)	1	0.779	0.7788	0.18	0.688	0.57
Bore depth (mm)*Bore depth (mm)	1	2.756	2.7561	0.63	0.457	2.00
2-Way Interaction	10	14.209	1.4209	0.33	0.943	10.32
Minor radius (mm)*Major radius (mm)	1	5.870	5.8698	1.34	0.290	4.26
Minor radius (mm)*Height (mm)	1	3.850	3.8496	0.88	0.384	2.80
Minor radius (mm)*Fillet radius (mm)	1	0.011	0.0108	0.00	0.962	0.01
Minor radius (mm)*Bore depth (mm)	1	0.006	0.0058	0.00	0.972	0.00
Major radius (mm)*Height (mm)	1	1.830	1.8298	0.42	0.542	1.33
Major radius (mm)*Fillet radius (mm)	1	0.434	0.4338	0.10	0.763	0.32
Major radius (mm)*Bore depth (mm)	1	1.843	1.8432	0.42	0.540	1.34
Height (mm)*Fillet radius (mm)	1	0.348	0.3485	0.08	0.787	0.25
Height (mm)*Bore depth (mm)	1	0.000	0.0000	0.00	0.998	0.00
Fillet radius (mm)*Bore depth (mm)	1	0.017	0.0174	0.00	0.952	0.01
Error	6	26.218	4.3697			19.04
Total	26	137.702				

Table 7 presents the results of the ANOVA analysis of the regression model for SIF (P15). The highest F-value of 578.68 was obtained for the input parameter height (P10). This value corresponds to $p = 0.000$, implying the rejection of H0 with 95% confidence ($p < 0.05$). The parameter height (P10) has the highest significance on SIF (P15), indicating that the variance explained by SIF (P15) is significantly larger than the unexplained variance in the model. Height is the most dominant factor influencing the SIF. This observation is consistent with the principles of mechanical engineering, as the transition region height is directly associated with the stress distribution near the discontinuity. A greater height results in

sharper transitions and higher stress concentration at the discontinuity. This observation is consistent with classical fracture mechanics, where geometric discontinuities significantly alter the local stress fields, thereby increasing the SIF [68]. Increased height-to-thickness ratios in stepped specimens increase the mode I SIF due to the constraint effects on the crack front. Therefore, the high statistical significance of height on SIF is validated from both statistical and mechanical perspectives. Other quadratic terms, P10P10 and P17P17, are also statistically significant, with p-values of 0.020 and 0.036, respectively. The statistical significance of these terms reflects the existence of non-linear relationships between these geometric parameters and the SIF (P15). Physically, a statistically significant height×height value indicates non-linear amplification of SIF with vertical dimensions of the stepped bar's transition zone. Similarly, a statistically significant Bore depth×depth term suggests a non-linear relationship between bore depth and SIF. This observation is attributed to stress redistribution around the crack front resulting from local thickness variations. These findings coincide with previous studies on the geometric sensitivity of fracture mechanics parameters [69]. The significant statistical quadratic terms collectively represent the second-order influence of geometric features on local stress fields.

Parameters minor radius (P7) and height^2 (P10^2) also exhibit p=0.005 and 0.020, indicating that these factors explain the model's 99.5% and 98% variance. Percentage contribution, in addition to the p- and F-values, facilitates a better understanding of the influence of geometric parameters. The percentage contribution column identifies the height (P10) as the most influential geometrical parameter, contributing more than 89.6%. It is followed by the minor radius (P7) and fillet radius (P16), with contributions of 2.94% and 2.25%, respectively. Conversely, terms such as major radius (P9), bore depth (P17), and most of the interaction terms contribute negatively, with a contribution < 1%. These findings suggest the possibility of model simplification by eliminating the terms that contribute the least to the model's accuracy.

Table 7. ANOVA table for response parameter SIF (P15)

Source	DF	Adj SS	Adj MS	F-Value	P-Value	% Contribution
Model	20	251082	12554	32.00	0.000	99.07
Linear	5	240496	48099	122.59	0.000	94.89
Minor radius (mm)	1	7442	7442	18.97	0.005	2.94
Major radius (mm)	1	239	239	0.61	0.465	0.09
Height (mm)	1	227047	227047	578.68	0.000	89.59
Fillet radius (mm)	1	5698	5698	14.52	0.009	2.25
Bore depth (mm)	1	70	70	0.18	0.687	0.03
Square	5	7127	1425	3.63	0.074	2.81
Minor radius (mm)*Minor radius (mm)	1	105	105	0.27	0.623	0.04
Major radius (mm)*Major radius (mm)	1	2028	2028	5.17	0.063	0.80
Height (mm)*Height (mm)	1	3908	3908	9.96	0.020	1.54
Fillet radius (mm)*Fillet radius (mm)	1	0	0	0.00	0.983	0.00
Bore depth (mm)*Bore depth (mm)	1	2863	2863	7.30	0.036	1.13
2-Way Interaction	10	3460	346	0.88	0.591	1.37
Minor radius (mm)*Major radius (mm)	1	114	114	0.29	0.610	0.04
Minor radius (mm)*Height (mm)	1	891	891	2.27	0.182	0.35
Minor radius (mm)*Fillet radius (mm)	1	0	0	0.00	0.996	0.00
Minor radius (mm)*Bore depth (mm)	1	311	311	0.79	0.407	0.12
Major radius (mm)*Height (mm)	1	343	343	0.87	0.386	0.14
Major radius (mm)*Fillet radius (mm)	1	414	414	1.05	0.344	0.16
Major radius (mm)*Bore depth (mm)	1	202	202	0.51	0.500	0.08
Height (mm)*Fillet radius (mm)	1	557	557	1.42	0.278	0.22
Height (mm)*Bore depth (mm)	1	465	465	1.19	0.318	0.18
Fillet radius (mm)*Bore depth (mm)	1	163	163	0.42	0.543	0.06
Error	6	2354	392			0.93
Total	26	253436				

The potential over-parametrisation of CCD-based regression models can be addressed using various established reduction techniques to enhance their parsimony. 'Backward elimination' is a widely employed reduction technique that involves systematically eliminating insignificant terms from the model. Another method, 'stepwise regression,' involves a combination of forward and backward selection-based criteria to iteratively eliminate predictor variables. Another crucial reduction technique, 'variance-based elimination', involves systematic elimination of terms contributing < 1% (threshold value) of the total variation. These terms must be checked for statistical significance before elimination from the model. In cases involving prioritised model prediction, the cross-validation techniques must be employed to aid in term elimination while maintaining the model's generality. However, the hierarchical model structure should be preserved

during the reduction to avoid any unintentional modelling bias. For example, the interaction terms must not be retained while eliminating the associated main effects. These reduction strategies are well-documented in the literature and have been successfully applied across various engineering fields [70].

The Pareto chart of standardised effects is used to visualise the influence of various factors on the response variables. It helps rank the factors' significance in impacting the response variable. The most influential factor can be identified using the Pareto charts. The vertical (dotted) line represents the threshold, and the length of each horizontal bar indicates the relative importance of the factor. Factors extending beyond the threshold line are understood to have a statistically significant effect on the response variable. Figure 9 (a) & (b) present the Normal and Pareto charts of the standardised effect of input factors on the response parameter crack extension (P12). As shown in Figure 9(a), the normal probability plot indicates that the data points are aligned with the reference line, suggesting a normal distribution. While most of the effects follow a quasi-linear trend, a few points located in the upper right corner show a remarkable deviation. These deviations might be attributed to the potential outliers, but can also be associated with physically meaningful observations. Factors such as height (P10), minor radius (P7), and fillet radius (P16) exhibit strong candidacy due to their considerable influence on geometry and stress concentration. For example, as previously discussed, the transition zone height has a significant influence on stress concentration and, consequently, crack growth. Similarly, a crack minor radius or fillet radius can alter the stress fields and accelerate the crack extension. In totality, these deviations are not artifacts but represent the key effects governing the fracture behaviour. Therefore, these deviations should be interpreted as indicators of critical geometric influences instead of statistical anomalies.

Statistically speaking, these minor deviations are acceptable and have a negligible effect on the analysis. The Pareto chart in Figure 9 (b) displays the most influential factor, height (P10). Only height (P10) crosses the threshold value of 2.447, implying that it is the sole factor affecting the crack extension in the stepped bar. The vertical reference line at 2.447 represents the critical t-value used to obtain the statistical significance at the selected confidence level. It corresponds to a two-tailed t-distribution at $\alpha = 0.05$ derived from the ANOVA table. Any bar crossing this vertical threshold indicates a term with a standardised effect exceeding that expected by chance. Such terms can be marked as statistically significant. This threshold is crucial for demarcating the truly influential terms from the less influential ones.

Figure 9 (c) shows the residual plots employed to check the validity of the model assumptions for the response parameter height (P10). The residuals represent the difference between observed and predicted values, and their level of randomness indicates whether the model is a good fit. The normal probability plot shows a scatter of points along a straight line, indicating the normal distribution of values. The residual versus fitted values plot depicts a random scattering of points, indicating a constant variance across the range of fitted values. The random scattering around the zero line indicates that the linearity assumption is valid. The absence of any particular pattern suggests that the model fits the predicted value range. It also represents the independence of residuals from the predictor. The frequency versus residuals histogram indicates a relatively random residual distribution, implying a departure from normality. The uneven spread of residual in the versus fit and versus order plots for crack extension (P12) reflects heteroscedasticity. This heteroscedasticity may affect the reliability of the statistical inferences. The issue is acknowledged but not addressed in the present investigation. The model was retained in its current form to maintain consistency with the initial experimental design and regression analysis. However, this issue of non-constant variance may be addressed by implementing variance-stabilizing transformations. These transformations identify the optimal power transformation for variance stabilizing and enhancing the normality. Future work may explore these variance-stabilizing transformations for handling such issues and improving the model's robustness and compliance with assumptions. The transformation of the response variable in regression modelling and normality approximation can be performed by the Box-Cox transformation. It can transform the non-constant variance observations by making the distribution closer to the normal [71]. Box-Cox transformations simplify the linear model, improving its interpretability.

The normal plot, Pareto chart, and residual plots for the influence of the input factors on the response parameter SIF (P15) are presented in Figure 10 (a)-(c). As shown in Figure 10 (a), the alignment of most data points along a straight line suggests that they follow a normal distribution. The factors C, A, D, CC, and EE significantly influence the SIF, as they cross the threshold value of 2.45 (see Figure 10(b)). As per the order of influence, these factors can be arranged as height (P10)>minor radius (P7)>fillet radius (P16)>height (P10)×height (P10)>bore depth (P17)×bore depth (P17). Figure 10 (c) shows that the residual plots were employed to explain the regression model's validity for the response parameter SIF (P15). The randomness in the residual and fitted values indicates the model's goodness of fit. The scatter of residuals along the straight line also suggests that they follow a normal distribution. The versus order plot also exhibits the absence of any identifiable pattern, indicating that the results are random and independent of the predictors.

Interestingly, the residual diagnostics for SIF (P15) exhibit significantly better statistical behaviour vis-à-vis the crack extension (P12). In the case of P15, the residuals follow a quasi-normal distribution with smaller skew. The residuals versus order and residual versus vits plots indicate random scatter without apparent patterns, suggesting homoscedasticity. The histogram for SIF (P15) also depicts a relatively symmetric spread centred around zero as compared with the histogram for crack extension (P12). The better statistical performance of SIF (P15) might be due to the physical nature of SIF. The SIF is an energy-based, deterministic fracture parameter that is determined by the loading configuration and geometry. Numerical and analytical models can represent it and are less affected by microstructural variability and local plasticity [72]. Conversely, crack extension is considered relatively more complex, path- and mesh-dependent, rendering

it challenging to capture through second-order modelling. However, residual stresses have been shown to accelerate the crack propagation under fatigue loading by approximately 50% [73].

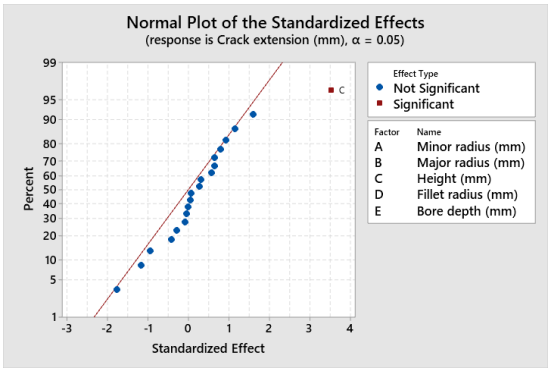

(a)

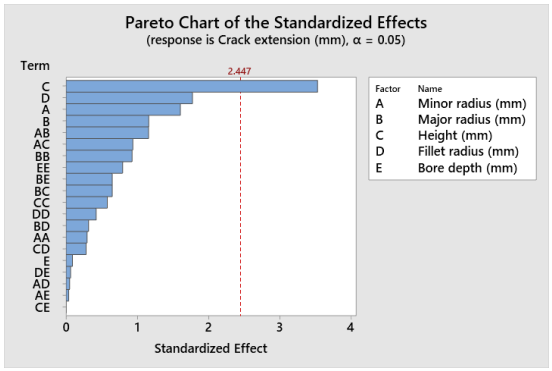

(b)

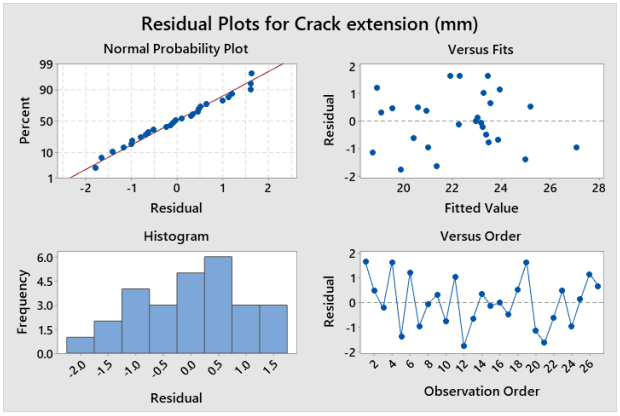

(c)

Figure 9. (a) Normal plot, (b) Pareto chart of the standardised effects, and (c) residual plots for crack extension (P12)

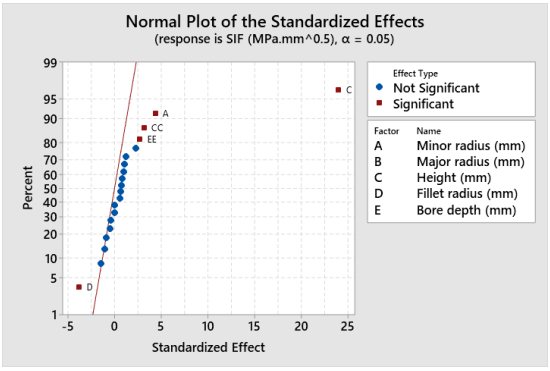

(a)

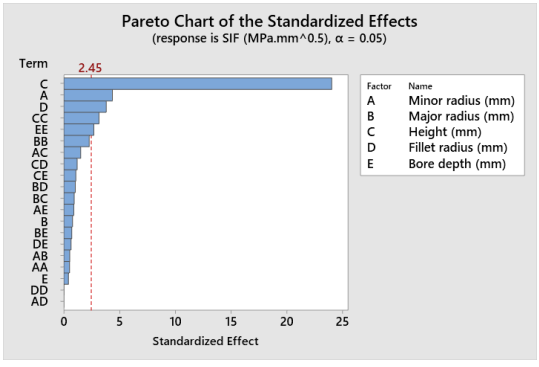

(b)

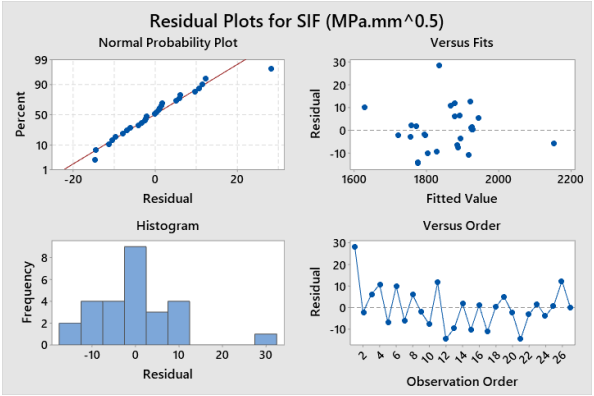

(c)

Figure 10. (a) Normal plot, (b) Pareto chart of the standardised effects, and (c) residual plots for SIF (P15)

5.2.2 Main Effects and Interaction Plots

The main effects plots help visualise the influence of various factors on the response variable. It depicts the variation in the response variable when the factor value is changed from one level to another, averaged over the other factor levels. Figure 11 (a)-(e) illustrates the main effect plot, depicting the individual effects of input factors major radius (P9), minor radius (P7), height (P10), fillet radius (P16), and bore depth (P17) on the response parameter, crack extension (P12). The non-zero starting vertical axis was chosen to improve the visibility of the magnitude at different factor levels. This choice is deliberate, given the narrow range between the extreme values of 19 mm and 26 mm, as well as slight variations in factors other than height (P10). A full zero-based axis would compress the vertical variation, concealing the differences between different factor levels. Moreover, consistent scale and range across all factors ensure visual uniformity and prevent misrepresentation. Such practice is common where the non-overlapping intervals support the statistical significance.

The inclusion of a confidence interval in the main effects plot helps differentiate between the actual and physical effects and sampling variability-induced fluctuations [64]. These plots represent the visualisation of the influence of geometric parameters on the crack extension (P12). Among all the variables, height (P10) is the most influential and statistically significant parameter. Figure 11 (a) reveals an increase in the crack extension with height, with non-overlapping confidence intervals. This behaviour confirms the robustness of the underlying influence and highlights stable crack growth in higher geometries. Conversely, the minor radius (P7) exhibits a moderate influence with a minor peak at the mid-level. The overlapping error bars in this case indicate a lower statistical significance for the minor radius (P7) compared to the height (P10). Other parameters, including major radius (P9), fillet radius (P16), and bore depth (P17), exhibit relatively flat trends with overlapping confidence intervals. This reveals a statistically insignificant influence of these parameters on the crack extension [74]. The dominant role of height (P10) in governing crack propagation suggests future design optimisation studies should prioritise this parameter over others.

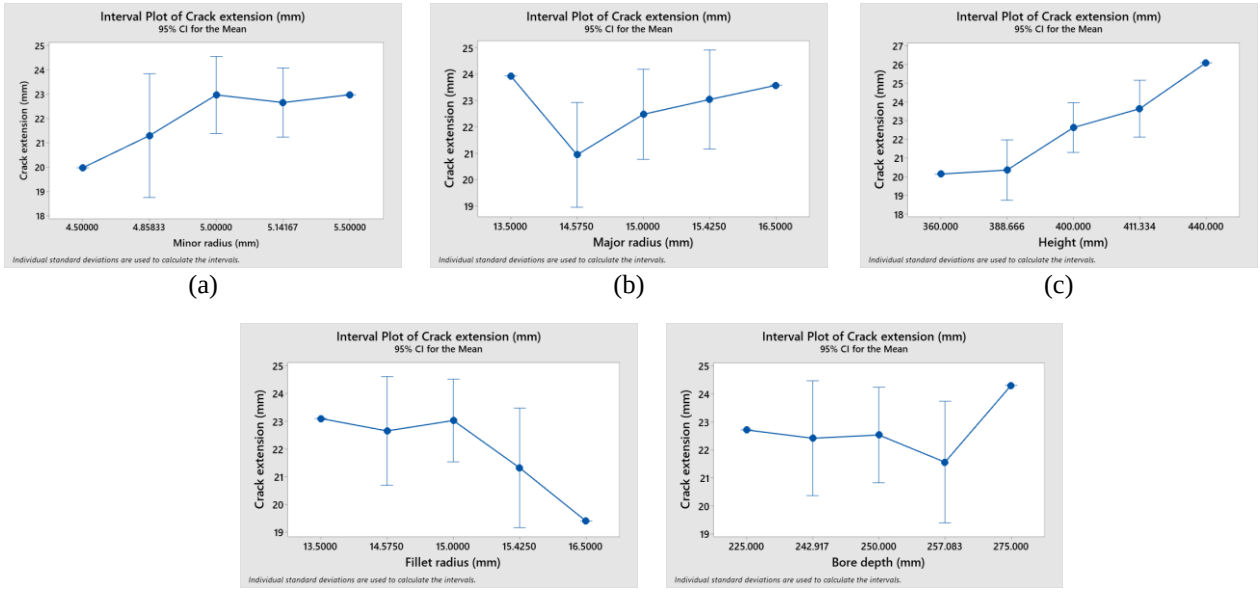

(a) (b) (c)

(d) (e)

Figure 11. Main effects plot for crack extension (P12) with (a) minor radius (P7), (b) major radius (P9), (c) height (P10), (d) fillet radius (P16), and (e) bore depth (P17)

Figure 12 (a)-(e) illustrates the main effect plot, depicting the individual effect of input factors on the response parameter SIF (P15), along with a 95% confidence interval. As shown in Figure 12 (a), the monotonic increase in SIF with height (P10) identifies it as the most influential and statistically significant parameter. This observation is consistent with the classical fracture mechanics approach, where higher samples will exhibit a higher SIF under flexural loading. The non-overlapping confidence intervals across different height levels demonstrate the statistical significance of height (P10) compared to other parameters. Conversely, other factors, including minor and major radii (P7, P9), fillet radius (P16), and bore depth (P17), exhibit relatively flat or non-symmetric trends with overlapping confidence intervals (see Figure 12 (c-e)). This observation suggests statistical insignificance as compared to height [74]. Interestingly, the main effects plot for height (P10) shows linear effects between height and SIF (P15), contrary to the classical fracture mechanics perspective. The trend is evident visually and supported by the non-overlapping confidence intervals across all the levels considered. In fracture mechanics, the geometric features show a non-linear relationship with the fracture parameters due to complex interactions among them. This non-linear relationship arises from the complex interactions among constraints, crack front curvature, and the stress triaxiality. In real life, the stress intensity at a discontinuity is influenced by the height of flexurally loaded samples. The observed linearity may be attributed to the restricted design space and well-controlled boundary conditions, which suppress interaction effects at the crack tip. These observations suggest that while the analytical models may yield non-linearity between height (P10) and SIF (P15), practical behaviour can approximate a linear response between them.

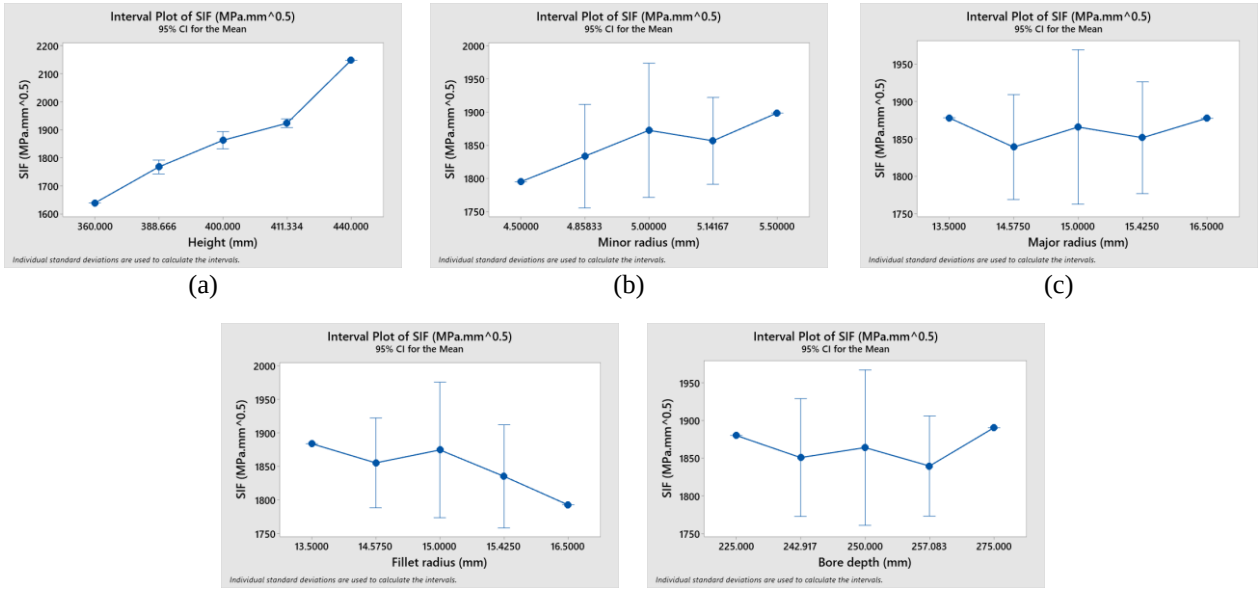

Figure 12. Main effects plot for SIF (P15) with (a) minor radius (P7), (b) major radius (P9), (c) height (P10), (d) fillet radius (P16), and (e) bore depth (P17)

An interaction plot helps represent the interaction effects between two factors on the response variable. It interprets the interaction between these factors by plotting their value at different levels against the response variable. Parallel lines indicate no interaction, while non-parallel lines indicate interaction among the factors. Likewise, intersecting lines manifest a strong interaction between the factors. The results of ANOVA for crack extension crack extension (P12) presented in Table 6 reveal that none of the two-way interaction terms are statistically significant. The p-values for all interaction terms range between 0.29 and 0.998, with each contributing less than 4.3% of the total variance. This finding suggests the dominance of main effects, such as height (P10), which accounts for 39.6% of the total variance with a p-value of 0.012. However, from a fracture mechanics perspective, some geometric combinations may exhibit a coupling effect on crack growth. These coupling effects are amplified in the presence of constrained 3D loading, like in the present case.

For example, the minor radius × height pairing (P7 × P10), while statistically insignificant (p = 0.384), may influence the crack front development in cylindrical stepped components [68]**.** Similarly, the minor radius × major radius coupling (P7 × P9) has a p-value of 0.88 and is the second-most statistically significant interaction effect. The interaction between the minor and major radii of the crack determines the semi-elliptical crack's aspect ratio. The aspect ratio of the crack plays a crucial role in defining the shape of the crack front. The aspect ratio influences the SIF distribution along the crack front, ultimately dictating the crack path and curvature. Figure 13 (a) & (b) shows the interaction plots depicting the effect of various interaction terms in the ANOVA modelling on crack extension (P12). As shown in Figure 13 (a), the P7×P10 plot exhibits a uniform increase across all minor radius levels. This effect is more pronounced at higher minor radius values. The lines exhibit non-parallel trends, indicating a strong interaction between the variables and their influence on crack extension. In a physical sense, this implies a synergistic relationship between the height and minor radius, amplifying the stress concentration under flexural loading. This observation reinforces the fact that the local geometry plays a vital role in determining fracture initiation in notched bodies [75]. Figure 13 (b) illustrates the interaction plots for minor and major radii (P7×P9) and their influence on the crack extension. The lines exhibit non-parallel trends, indicating the existence of interaction effects. The plot suggests that a change in the crack's aspect ratio affects the stress distribution along the crack front, ultimately altering the crack extension [62].

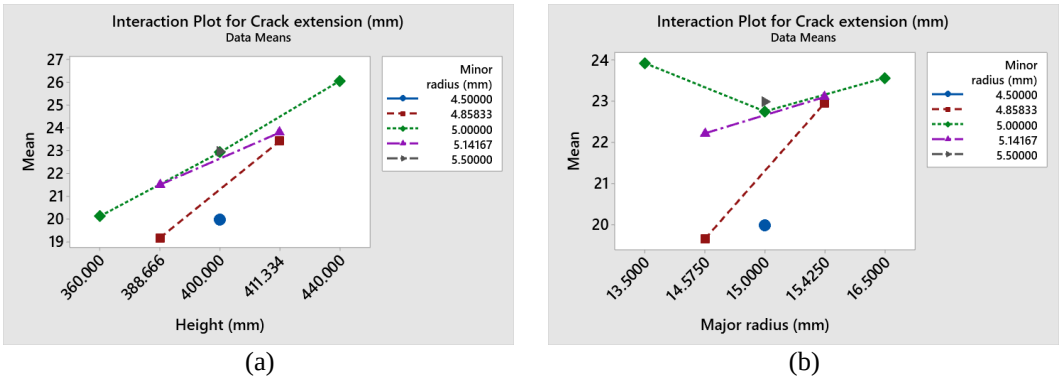

Figure 13. Interaction plots for (a) minor radius×height (P7×P10) and (b) minor radius×major radius (P6×P7) for crack extension (P12)

Based on the ANOVA results for SIF (P15) presented in Table 7, the top two statistically significant interaction effects were identified for further analysis. These two interaction effects are the minor radius × height (P7 × P10) and height × fillet radius (P10 × P16), with p-values of 0.182 and 0.278, respectively. Although these values are greater than the $p < 0.05$ threshold, they still hold significance from a fracture mechanics perspective. Figure 14 (a) & (b) depicts the interaction plots for visualizing the influence of various factors on the response variable SIF (P15). As shown in Figure 14 (a), the P7×P10 interaction plot exhibits a divergent trend, particularly at higher crack depths. This divergent trend indicates a strong interaction between the two parameters. Similar to the previous case (P12), the increase remains unchanged at all the minor radius levels. However, the SIF achieves maximum value for a minor radius of 5 mm and a height of 440 mm. Conversely, the P10×P16 interaction plot displays relatively parallel lines across all height levels, indicating minimal interaction (see Figure 10 (b)). The trends remarkably show an absence of interaction between the fillet radius and height and their inability to alter the SIF. Such trends might be attributed to the consistent stress-mitigating role of the fillet radius across all the height levels.

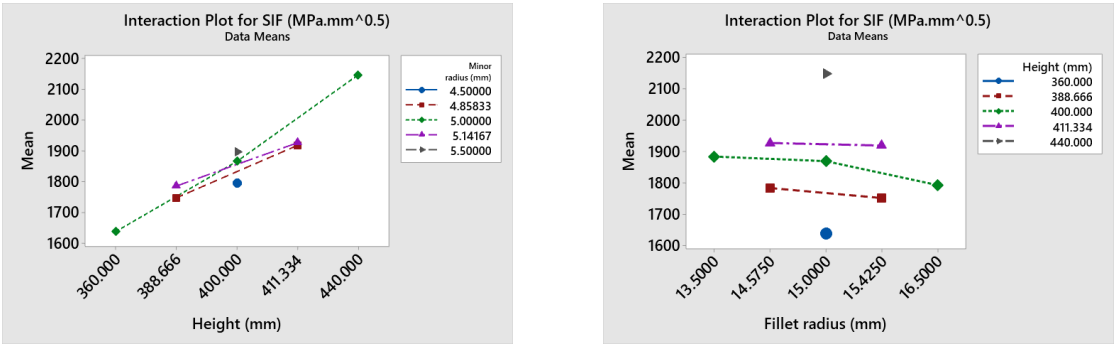

(a) (b)

Figure 14. Interaction plots for (a) minor radius × height (P7×P10) and (b) minor radius × fillet radius (P7×P16) for SIF (P15)

5.2.3 Contour Plots

Contour plots for the response variable crack extension (P12) and the five input parameters (minor radius (P7), major radius (P9), height (P10), fillet radius (P16), and bore depth (P17)) are presented in Figure 15 (a)-(j). Figure 15 (a) and (b) illustrate the effect of minor radius (P7), major radius (P9), and height (P10) on crack extension (P12) when all the other parameters are held constant. The value of crack extension (P12) increases with the minor radius (P7) and major radius (P9) values approximately equal to 5.50 mm and 13.5 mm, respectively (see Figure 15 (a)). As shown in Figure 15 (b), the highest value of SIF (P15) (> 30 mm) was observed for the highest value of height (P10). On the other hand, the minimum value of crack extension (P12) was obtained for the lowest height (P10) and minor radius (P7) values. Similar trends were noticed in the input factor bore depth (P17) (Figure 15 (b)). Figure 15 (c) and (d) present the contour plots for the influence of minor radius (P7), fillet radius (P16), and bore depth (P17) on the response variable crack extension (P12). It is evident in Figure 15 (c) that a higher minor radius (P7) value is associated with the highest crack extension (P12) value (> 24 mm). On the contrary, the lowest value (< 18 mm) is observed with the lowest minor radius (P7) and the highest fillet radius (P16) value (extreme left top corner). For the lowest minor radius (P7) value (~4.5 mm), bore depth (P17) values ranging from 235-265 mm result in the lowest crack extension (P12) value, provided all the other input parameters are held at constant values (see Figure 15 (d)). Similarly, minor radius (P7) and height both have a noticeable influence on crack extension (P12). This influence is evident in Figure 15 (e), illustrating that a higher value of major radius (P9) and lower height (P10) decrease the crack extension (P12) to < 20 mm. As shown in Figure 15 (f), a higher fillet radius (P16) value and a lower major radius (P9) value manifest in a smaller crack extension (P12) value in the top left corner. This finding indicates a reduction in the stress concentration due to a larger fillet radius, resulting in a smaller crack extension.

As shown in Figure 15 (g), an increase in the input parameter bore depth (P17) value, combined with a smaller major radius (P9), also results in a smaller crack extension (P12) < 20 mm. The minimum value is evident from the top left corner of the contour plot. As expected, combining the highest values of these variables yields the highest crack extension (P12), which exceeds 25 mm. These highest values are at the right corner of the contour plot presented in Figure 15 (h). The contour plot illustrating the impact of height (P10) and bore depth (P17) on crack extension (P12) is presented in Figure 15 (i). Uniform thickness contour bands represent the continuous increase in the crack extension (P12) with the height (P10). The highest values of crack extension (P12) (< 28 mm) were observed at the top and bottom corners of the rightmost corner. On the other hand, the lowest crack extension (P12) value (<20 mm) was obtained between the bore depth (P17) values, which ranged approximately from 225 to 275 mm. Figure 15 (j) presents the contour plot corresponding to the influence of the fillet radius (P16) and bore depth (P17) on the response variable crack extension (P12). It is clear that combining a higher value of fillet radius (P16) and bore depth (P17), which ranges approximately from 225 to 265 mm, results in a smaller crack extension (P12) value (< 20 mm).

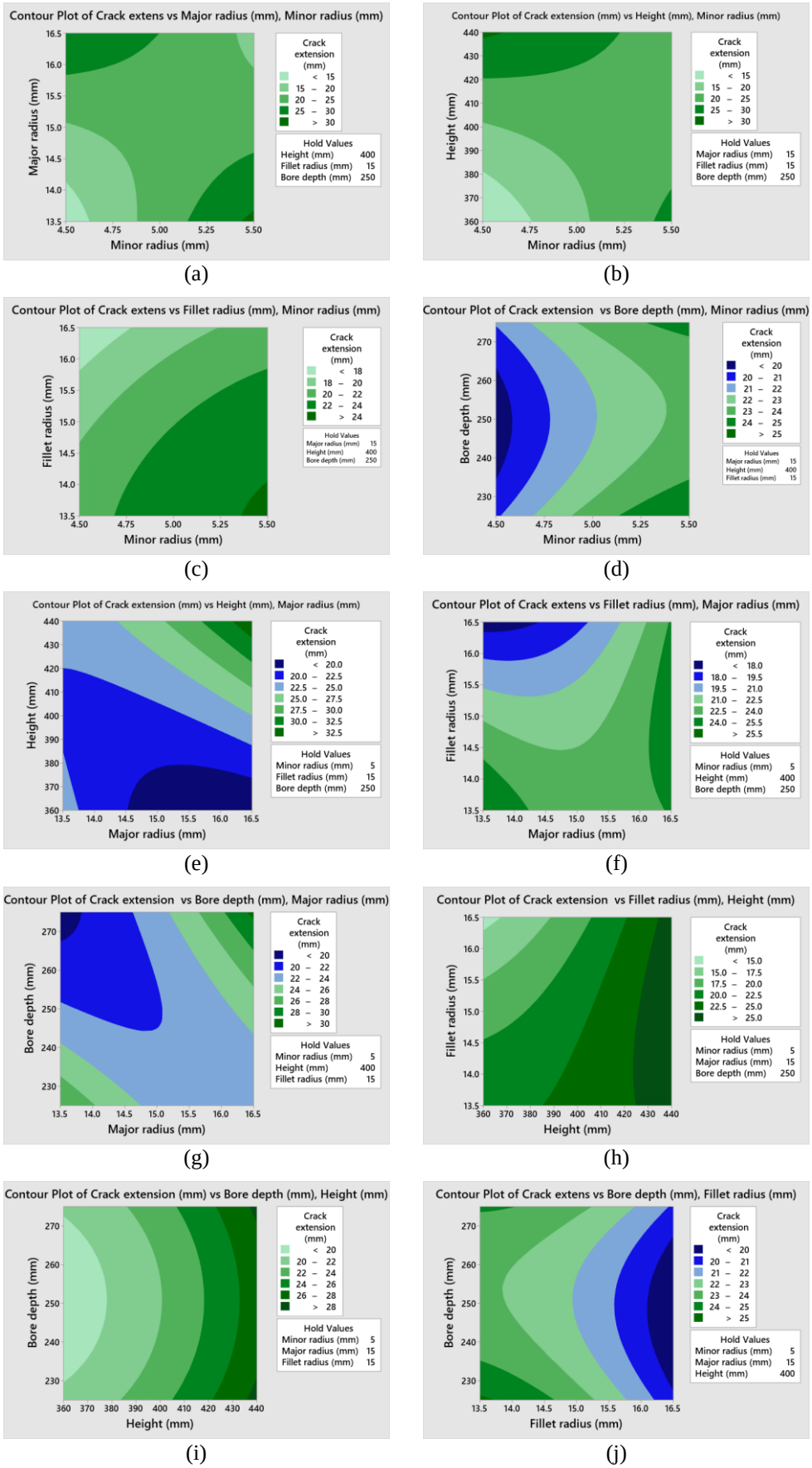

Figure 15. Contour plots for response variable crack extension (P12) and (a) minor radius (P7), major radius (P9), (b) minor radius (P7), height (P10), (c) minor radius (P7), fillet radius (P16), (d) minor radius (P7), bore depth (P17), (e) major radius (P9), height (P10), (f) major radius (P9), fillet radius (P16), (g) major radius (P9), bore depth (P17), (h) height (P10), fillet radius (P16), (i) height (P10), bore depth (P17) and (j) fillet radius (P16), bore depth (P17)

As shown in Figure 15(a), the contour plot for the crack extension (P12) versus minor radius (P7) and major radius (P7) interaction indicates non-monotonic transitions, suggesting a nonlinear interaction between the factors. The saddle-shaped contour plot reveals higher crack extension when the individual radius is altered individually rather than simultaneously. Mechanically, such behaviour emerges from the fact that the crack front geometry (minor and major radii of the semi-elliptical crack) manipulates the local SIF. A deeper crack with a larger minor radius increases the SIF near the crack centre, whereas a longer surface crack with a larger major radius extends the high-stress zone. With both radii at their higher sides, the crack front flattens, mitigating the stress concentration due to the stress-shielding effects [76].

The contour plots for crack extension (P12) versus minor radius (P7) and height (P10) interaction reveal a remarkable interaction between the variables. The crack extension increases significantly as the specimen height and minor radius increase. The transition from light to dark shades along the diagonal of the contour space reflects strong interaction effects. The crack geometry, such as curvature, has a significant influence on crack growth. A sharper notch leads to rapid crack initiation and high-speed propagation [77]. In the present case, a larger minor semi-elliptical surface crack radius implies a deeper crack, increasing the local SIF at the discontinuity. When combined with a taller geometry (considerable height), the structure undergoes greater bending moment and constraint effects. These synergistic effects amplify the crack-driving forces, promoting greater crack extension.

Figure 16 (a)-(j) illustrates the contour plots for the variation in the response variable SIF (P15) and the five input variables (minor radius (P7), major radius (P9), height (P10), fillet radius (P16), and bore depth (P17)). The contour plots are invaluable in visualizing the key trends and interactions between the input and response variables. Figure 16 (a) displays the effect of input parameters minor radius (P7) and major radius (P9) on the response variable, with the remaining variables held at mid-level values. The increase in SIF (P15) with minor radius (P7) reaching a maximum value of > 1950 MPa√mm was observed in the bottom rightmost location (minor radius (P7) is at the highest value). Contrarily, the SIF (P15) values are smaller towards the left of the contour plot at lower values of minor radius (P7) and major radius (P9). Figure 16 (b) depicts the contour plot of minor radius (minor radius (P7)), height (P10), and the response variable SIF (P15) with the other factors held at constant values. The highest value of SIF (P15) (> 2100 MPa√mm) was observed at the left top, indicating the critical effect of height (P10) on the response variable. A strong interaction between height (P10) and SIF (P15) can be discerned from the Figure. The contour lines are almost equidistant, suggesting a steep increase in SIF (P15). The lowest value of SIF (P15) was observed at the lowest values of minor radius (P7) and height (P10) (bottom left corner). The contour plot between SIF (P15), minor radius (P7), fillet radius (P16), and minor radius (P7), bore depth (P17), and SIF (P15) holding other parameters at constant values, is presented in Figure 16 (c & d). The highest SIF (P15) value is obtained at the highest value of minor radius (P7) and the lowest value of fillet radius (P16).

Conversely, the lowest value (< 1760 MPa√mm) was observed at the lowest and highest values of minor radius (P7) and fillet radius (P16), respectively. Similarly, the highest value of SIF (P15) (> 1960 MPa√mm) was obtained at the highest and lowest values of minor radius (P7) and bore depth (P17), respectively. The minimum value of SIF (P15) (<1800 MPa√mm) was obtained for the minimum bore depth (P17) and minor radius (P7) values. As shown in Figure 16 (e) & (f), the combination of major radius (P9) and height (P10) yields the highest values of SIF (P15). Alternatively, the highest value of SIF (P15) was obtained for the lowest fillet radius (P16) and minor radius (P7) (>1960 (see Figure 16 (f)). A higher value of fillet radius (P16) and a lower value of major radius (P9) yield the lowest value (<1800 MPa√mm). Interestingly, as shown in Figure 15 (g) and (h), bore depth (P17) and major radius (P9) exhibit unique contour plots, indicating that the lowest value of SIF (P15) (<1850 MPa√mm) is observed for the central, 'oval'-shaped region. This value increased to >2100 MPa√mm for the rightmost bottom corner in the case of height (P10) and fillet radius (P16) (see Figure 16 (h)). Figure 16 (i) and (j) present the contour plots for the input parameters bore depth (P17), height (P10), and fillet radius (P16). It is evident that at higher values of height (P10), the maximum values of SIF (P15) (>2200 MPa√mm) are obtained. Conversely, smaller bore depths (P17) and fillet radii (P16) yield maximum values of SIF (P15) (>1950 MPa√mm). In this case, the minimum SIF (P15) value (<1950 MPa√mm) was obtained for the highest fillet radius (P16) and bore depth (P17) values, which ranged between 230 mm and 250 mm.

The contour plots for SIF (P15) versus height (P10) and minor radius (P7) reveal distinct SIF responses due to geometric interaction effects. As expected, the SIF increases with both height and minor radius, manifesting the increase in SIF with crack curvature and specimen height. As explained earlier, a greater height contributes to higher flexural stress at the transition region of the stepped bar, significantly increasing the SIF. Similarly, in the presence of a plain-strain constraint, deeper cracks with a larger minor radius result in higher stress triaxiality and, consequently, a higher SIF value. Similar higher stress concentration and SIF have been observed in the case of concave weld beads [77]. While easier to fabricate, a concave weld shape is not favourable for achieving high-strength welds. As shown in Figure 16 (i), the SIF (P15) versus height (P10) and bore depth (P17) contour plots reveal fascinating insights into the influence of height and bore depth on the SIF. An increase in the SIF can be observed at larger heights and smaller bore depths. However, an increase in the bore depth diminishes the SIF, and the plateauing effect is visible at larger heights. Mechanically, deep bores reduce the net cross-sectional area, introducing localised stress concentrations. But the taller sections result in stress distribution across the section, diminishing this effect [78].

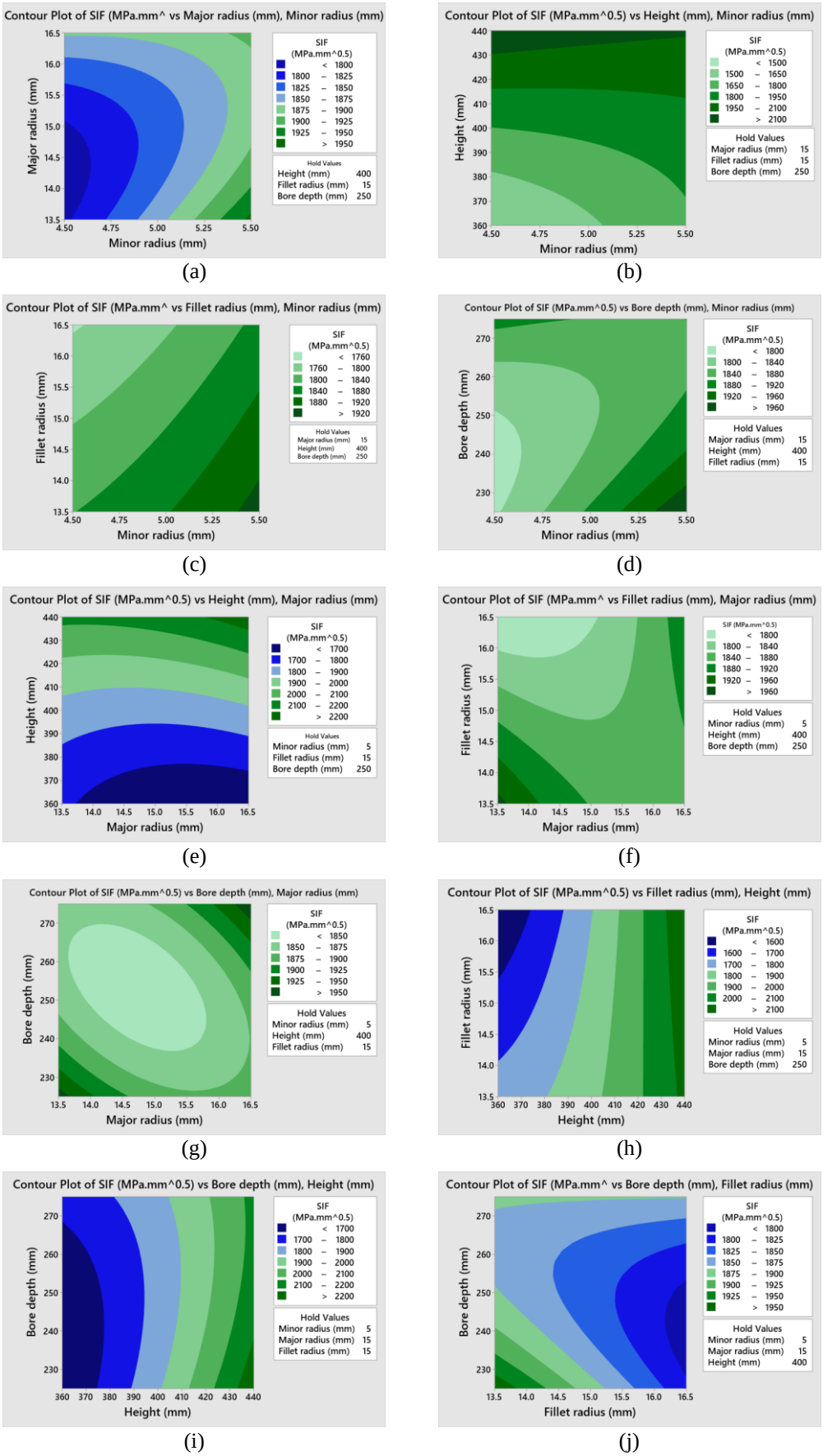

Figure 16. Contour plots for response variable SIF (P15) and (a) minor radius (P7), major radius (P9), (b) minor radius (P7), height (P10), (c) minor radius (P7), fillet radius (P16), (d) minor radius (P7), bore depth (P17), (e) major radius (P9), height (P10), (f) major radius (P9), fillet radius (P16), (g) major radius (P9), bore depth (P17), (h) height (P10), fillet radius (P16), (i) height (P10), bore depth (P17) and (j) fillet radius (P16), bore depth (P17)

6. CONCLUSIONS

The present investigation explores the influence of multiple geometric parameters on crack extension and SIF in a cracked stepped bar under flexural loading. The model was discretised into 49635 finite elements after the mesh independence test and simulated under flexural loading using ANSYS WB. The key novelty of the study lies in integrating SMART with the CCD approach. While the SMART ensures accurate static crack growth modelling, the CCD facilitates practical statistical analysis of the design space with twenty-seven simulations.

For the initial geometry, FEA revealed the highest von Mises stress, SIF, and crack extension of 947.13 MPa, 1864.20 MPa√mm, and 23.56 mm, respectively. Due to the absence of any analytical or published benchmarks for specific stepped bars with similar geometric and boundary conditions, the FEA results were carefully verified through mesh independence testing. The results were validated by mesh independence testing to establish confidence in the numerical results. The regression model developed could explain up to 80.96% and 99.07% variability. The most influential geometrical factors were identified using the Pareto and normal charts for the standardised effects and corresponding p-values. These charts identified height (P10) as the most influential factor affecting the crack extension (P12). In the case of the SIF (P15), the factors can be arranged in decreasing order of their influence as height (P10)>minor radius (P7)>fillet radius (P16)>height (P10)×height (P10)>bore depth (P17)×bore depth (P17). While the regression model performed satisfactorily for predicting SIF (P15), it exhibited poor predictive ability for crack extension (P12). This limitation arises from the complex, non-linear nature of the crack growth behaviour, which a second-order polynomial may not accurately capture. The interaction terms with slow statistical significance also reflect a potentially overfitted model. Future work may include the exploration of alternative modelling techniques and the expansion of datasets with additional simulations to capture the highly nonlinear responses. The main and interaction effects plots reveal interaction between the minor and major radii of the semi-elliptical cracks.

Moreover, the minor radius and height are the most influential interactions as far as crack propagation is concerned. These findings were further supported by contour plots that visualised the combined influence of parameter pairs while holding other variables constant. The contour plots revealed an increase in SIF with height and minor radius. A greater height contributes to increasing the bending moment and corresponding stress at the transition region, ultimately influencing the SIF. An increase in the SIF was also noted at higher heights and smaller bore depths, indicating stress redistribution near the crack due to smaller bore depths. From a design perspective, engineers and designers should focus on minimizing the surface crack's aspect ratio to mitigate stress concentration at the crack tip. Additionally, a taller height, combined with a deeper crack, may increase the SIF and crack extension. A careful control of the specimen geometry is crucial when designing stepped components, especially under fatigue applications. These insights provide a qualitative and quantitative overview to the engineers and designers involved in developing damage-tolerant components. These results offer insightful results into the broader aspects of fracture mechanics in cracked components with geometric discontinuities. The observed sensitivities of crack parameters to geometric features reinforce the importance of balancing component geometry with local stress concentration. These findings are scalable to other geometries, such as nozzles, shafts, and pressure vessels with semi-elliptical cracks. It offers a framework for predictive modelling and design optimisation of other industrial components with embedded or surface cracks.

While the present investigation provides important insights into the influence of geometric parameters of a cracked stepped bar under static flexural loading, several limitations should be acknowledged. The regression model exhibited limited predictive accuracy, especially for crack extension (P12). This suggests the need to employ more advanced surrogate modelling techniques to capture the highly nonlinear behaviour of fracture problems. Techniques such as artificial neural networks are capable of handling problems with non-linear relationships that are hard to describe analytically. The lack of experimental validation or benchmark data for the specific geometry used in the analysis limits the direct validation of the FE modelling. The study focuses on static loading conditions without considering fatigue or thermal effects. These effects are crucial for understanding the actual behaviour of the machine components. Future research should incorporate high-fidelity experimental and modelling approaches, such as cohesive zone modelling, to explore the influence of material behaviour under these loading spectra. The present analysis can be extended to different geometries and multi-material configurations to improve the generalizability and practical relevance of the fracture problems.

ACKNOWLEDGEMENTS

The author gratefully acknowledges the use of computational facilities and technical resources that supported the completion of this study.

FUNDING

This study was not supported by any grants from funding bodies in the public, private, or not-for-profit sectors.

CONFLICT OF INTEREST

The author declare no conflicts of interest.

AUTHORS' CONTRIBUTION

D. Gunwant (Conceptualisation; Formal analysis; Visualisation; Writing - original draft, Writing - final draft)

AVAILABILITY OF DATA AND MATERIALS

The datasets generated and/or analysed during the current study are available from the corresponding author on reasonable request.

ETHICS STATEMENT

This study did not involve human participants or animals. Ethical approval was therefore not required.

REFERENCES

[1] X. Zhang, "A case study of the collapse of the Interstate 35W Mississippi River Bridge," in *Proceeding of Fifth International Conference on Traffic Engineering and Transportation System (ICTETS 2021)*, vol. 12058, pp. 913–919, 2021.

[2] W. Seibel, "Intended ignorance: The collapse of the I-35W Mississippi River Bridge on 1 August 2007," in *Collapsing Structures and Public Mismanagement*. Cham, Switzerland: Springer, 2022, pp. 55–86.

[3] J. Huang, P. Fu, R. R. Settgast, J. P. Morris, F. J. Ryerson, "Evaluating a simple fracturing criterion for a hydraulic fracture crossing stress and stiffness contrasts," *Rock Mechanics and Rock Engineering*, vol. 52, no. 6, pp. 1657–1670, 2019.

[4] R. C. Neto, A. Akhavan-Safar, E. M. Sampaio, B. D. Simões, L. L. Vignoli, L. F. M. da Silva, "Creep behaviour of adhesively bonded joints: A comprehensive review," *Proceedings of the Institution of Mechanical Engineers, Part L: Journal of Materials Design and Applications*, vol. 238, no. 9, pp. 1625–1650, 2024.

[5] J. Xu, W. He, Z. Wang, T. Ding, Y. Liu, B. Wang, "An improved photoelastic method for determining stress intensity factors of rock-like material," *Theoretical and Applied Fracture Mechanics*, vol. 133, p. 104608, 2024.

[6] K. Yuan, J. Liu, "Two-dimensional weight function for determining stress intensity factors for semi-elliptical surface cracks in finite plates," *Theoretical and Applied Fracture Mechanics*, vol. 121, p. 103495, 2022.

[7] S. Chen, "General finite element methods with special focus on XFEM," in *Advanced Computational Methods and Geomechanics*. Singapore: Springer, 2023, pp. 325–392.

[8] S. The, A. Andriyana, S. Ramesh, I. S. Putra, P. Kadarno, J. Purbolaksono, "Tetrahedral meshing for a slanted semi-elliptical surface crack at a solid cylinder," *Engineering Fracture Mechanics*, vol. 241, p. 107400, 2020.

[9] P. Li, W. Li, B. Li, S. Yang, Y. Shen, Q. Wang, et al., "A review on phase-field models for fracture and fatigue," *Engineering Fracture Mechanics*, vol. 289, p. 109419, 2023.

[10] M. Salemi, H. Wang, "Fatigue life prediction of pipelines with equivalent initial flaw size using Bayesian inference," *Journal of Infrastructure Preservation and Resilience*, vol. 1, p. 3, 2020.

[11] K. Li, F. Wang, "A radial integration displacement discontinuity method for 3D fracture simulations," *Journal of Engineering Mathematics*, vol. 145, p. 1, 2024.

[12] J. Scheel, D. Wallenta, and A. Ricoeur, "A critical review on complex potentials in linear elastic fracture mechanics," *Journal of Elasticity*, vol. 147, no. 1–2, pp. 291–308, 2021.

[13] A. A. Tyrymov, "Numerical simulation of T-stresses and stress biaxiality factors for centrally cracked specimens," *Journal of Applied Mechanics and Technical Physics*, vol. 63, no. 7, pp. 1264–1271, 2022.

[14] D. C. Pham, X. Cui, X. Ren, J. Lua, "A discrete crack-informed 3D continuum damage model for delamination migration," *Composites Part B: Engineering*, vol. 165, pp. 554–562, 2019.

[15] H. Deng, B. Yan, X. Zhang, Y. Zhu, "A new enrichment scheme for interfacial crack modelling using XFEM," *Theoretical and Applied Fracture Mechanics*, vol. 122, p. 103595, 2022.

[16] V. B. Pandey, I. V. Singh, B. K. Mishra, "A continuum damage mechanics–XFEM framework for fatigue crack growth simulations," *Engineering Fracture Mechanics*, vol. 206, pp. 172–200, 2018.

[17] W. Yi, Q. Rao, S. Luo, Q. Shen, Z. Li, "Integral equation method for interacting stress intensity factors of multiple crack-hole problems," *Theoretical and Applied Fracture Mechanics*, vol. 107, p. 102535, 2020.

[18] Y. Li, K. Zheng, "Stress intensity factor analysis of kinked and hole cracks using numerical conformal mapping," *Theoretical and Applied Fracture Mechanics*, vol. 114, p. 103022, 2021.

[19] Y. S. Lo, M. J. Borden, K. Ravi-Chandar, C. M. Landis, "A phase-field model for fatigue crack growth," *Journal of the Mechanics and Physics of Solids*, vol. 132, p. 103684, 2019.

[20] A. V. M. Rocha, A. Akhavan-Safar, R. Carbas, E. A. S. Marques, R. Goyal, M. El-Zein, et al., "Numerical analysis of mixed-mode fatigue crack growth of adhesive joints using CZM," *Theoretical and Applied Fracture Mechanics*, vol. 106, p. 102493, 2020.

[21] A. M. Alshoaibi, Y. A. Fageehi, "Numerical analysis of fatigue crack growth path and life prediction," *Materials*, vol. 13, no. 15, p. 3380, 2020.

[22] P. Zhang, J. Li, Y. Zhao, J. Li, "Crack propagation analysis and fatigue life assessment of high-strength bolts," *Scientific Reports*, vol. 13, p. 1, 2023.

[23] A. M. Alshoaibi, Y. A. Fageehi, "Advances in finite element modelling of fatigue crack propagation," *Applied Sciences*, vol. 14, no. 20, p. 9297, 2024.

[24] N. Bisht, P. C. Gope, K. Panwar, "Influence of crack offset distance on interaction of multiple cracks," *Frattura ed Integrità Strutturale*, vol. 9, no. 32, pp. 1–12, 2015.

[25] P. C. Gope, N. Bisht, V. K. Singh, "Interaction of collinear and offset edge cracks," *Theoretical and Applied Fracture Mechanics*, vol. 70, pp. 19–29, 2014.

[26] Z. W. Wang, D. M. Li, Y. F. Zhong, Y. K. Liu, Y. N. Shao, "Review of experimental, theoretical and numerical advances in multi-crack fracture mechanics," *Mathematics*, vol. 12, no. 24, p. 3881, 2024.

[27] R. Bird, W. M. Coombs, S. Giani, "Adaptive configurational force-based crack propagation," *International Journal for Numerical Methods in Engineering*, vol. 123, no. 7, pp. 1673–1709, 2021.

[28] K. Schmitz, A. Ricoeur, "Configurational forces in 3D crack problems," *International Journal of Solids and Structures*, vol. 282, p. 112456, 2023.

[29] D. Rettenmaier, D Deising, Y Ouedraogo, E Gjonaj, H. De Gersem, D. Bothe, et al., "Load-balanced adaptive mesh refinement in OpenFOAM," *SoftwareX*, vol. 10, p. 100317, 2019.

[30] Y. P. Liu, T. J. Li, "VCCT using tetrahedral finite elements," *Engineering Fracture Mechanics*, vol. 253, p. 107853, 2021.

[31] H. Wu, R. R. Settgast, P. Fu, J. P. Morris, "An enhanced virtual crack closure technique for stress intensity factor calculation along arbitrary crack fronts and the application in hydraulic fracturing simulation," *Rock Mechanics and Rock Engineering*, vol. 54, no. 6, pp. 2943–2957, 2021.

[32] S. M. Nabavi, M. B. Shahmorady, "Stress intensity factors for semi-elliptical cracks in cylinders," *International Journal of Integrated Engineering*, vol. 12, no. 4, pp. 232–239, 2020.

[33] H. K. Thakur and G. Prasad, "Mixed-mode fracture behaviour of laminated structures," in *Fracture Behaviour of Nanocomposites and Reinforced Laminates*. Singapore: Springer, 2024, pp. 123–155.

[34] A. Subbaiah, R. Bollineni, "Stress intensity factor of inclined internal edge cracks," *Journal of Failure Analysis and Prevention*, vol. 20, no. 5, pp. 1524–1533, 2020.

[35] J. E. Rolón, E. D. Cendales, I. .M Cruz, "Computational two-dimensional modeling of the stress intensity factor in a cracked metallic material," *Journal of Physics: Conference Series*, vol. 687, p. 012070, 2016.

[36] N. Sukumar, D. L. Chopp, N. Moës, T. Belytschko, "Modeling holes and inclusions by level sets in the extended finite-element method," *Computer Methods in Applied Mechanics and Engineering*, vol. 190, nos. 46–47, pp. 6183–6200, 2001.

[37] S. Arunkumar, V. K. Nithin, "Stress intensity factor estimation for inclined centre cracks," *Journal of Failure Analysis and Prevention*, vol. 20, no. 6, pp. 2040–2058, 2020.

[38] J. Antony, *Design of Experiments for Engineers and Scientists*. Amsterdam, Netherlands: Elsevier, 2023.

[39] A. A. Pelegri, A. Tekkam, "Optimisation of laminate fracture toughness using DOE," *Journal of Composite Materials*, vol. 37, no. 7, pp. 579–596, 2003.

[40] S. J. S. Chelladurai, K. Murugan, A. P. Ray, M. Upadhyaya, V. Narasimharaj, S. Gnanasekaran, "Optimization of process parameters using response surface methodology: A review," *Materials Today: Proceedings*, vol. 37, pp. 1301–1304, 2021.

[41] F. Mouallem, G. F. Gomes, "Crack identification using RSM and neural networks," *Archive of Applied Mechanics*, vol. 91, no. 10, pp. 4389–4408, 2021.

[42] A. Jankovic, G. Chaudhary, F. Goia, "Designing the design of experiments (DOE) – An investigation on the influence of different factorial designs on the characterization of complex systems," *Energy and Buildings*, vol. 250, p. 111298, 2021.

[43] H. A. Kose, A. Yildizeli, S. Cadirci, "Parametric study and optimization of microchannel heat sinks with various shapes," *Applied Thermal Engineering*, vol. 211, p. 118368, 2022.

[44] J. H. Kim, T. Chau-Dinh, G. Zi, W. W. Lee, and J. S. Kong, "Probabilistic fatigue integrity assessment in multiple crack growth analysis associated with equivalent initial flaw and material variability," *Engineering Fracture Mechanics*, vol. 156, pp. 182–196, 2016.

[45] K. Chiranjeevi, D. H. Kumar, A. S. Srinivasa, A. U. Ravi Shankar, "Optimisation of recycled concrete aggregates for cement-treated bases by response surface method," *International Journal of Pavement Engineering*, vol. 24, no. 1, p. 2179051, 2023.

[46] L. Xu, P. Hu, Y. Li, N. Qiu, G. Chen, X. Liu, "Improved fatigue reliability analysis of deepwater risers based on RSM and DBN," *Journal of Marine Science and Engineering*, vol. 11, no. 4, p. 688, 2023.

[47] X. Long, L. Cai, W. Li, "RSM-based assessment of pavement concrete mechanical properties under joint action of corrosion, fatigue, and fiber content," *Construction and Building Materials*, vol. 197, pp. 406–420, 2019.

[48] S. Oza, P. Kodgire, S. S. Kachhwaha, "Analysis of RSM-based BBD and CCD techniques applied for biodiesel production from waste cotton-seed cooking oil via ultrasound method," *Analytical Chemistry Letters*, vol. 12, no. 1, pp. 86–101, 2022.

[49] A. Asfaram, M. Ghaedi, H. Abidi, H. Javadian, M. Zoladl, F. Sadeghfar, "Synthesis of Fe_3O_4@CuS@Ni_2P-CNTs magnetic nanocomposite for sonochemical-assisted sorption and pre-concentration of Allura Red: CCD-RSM design," *Ultrasonics Sonochemistry*, vol. 44, pp. 240–250, 2018.

[50] M. Ghanbari, A. M. Hadian, A. A. Nourbakhsh, K. J. D. MacKenzie, "Modeling and optimization of compressive strength and bulk density of metakaolin-based geopolymer using central composite design," *Ceramics International*, vol. 43, no. 1, pp. 324–335, 2017.

[51] E. Ding, C. Cao, H. Hu, Y. Chen, X. Lu, "Application of central composite design to the optimization of fly ash-based geopolymers," *Construction and Building Materials*, vol. 230, p. 116960, 2020.

[52] S. J. M. Breig, K. J. K. Luti, "Response surface methodology: Applications and challenges," *Materials Today: Proceedings*, vol. 42, pp. 2277–2284, 2021.

[53] NIST/SEMATECH, "Central composite designs (CCD)," *e-Handbook of Statistical Methods*. [Online]. Available: https://www.itl.nist.gov/div898/handbook/pri/section3/pri3361.htm. Accessed: Dec. 3, 2024.

[54] A. M. Alshoaibi, Y. A. Fageehi, "3D modelling of fatigue crack growth using ANSYS," *Ain Shams Engineering Journal*, vol. 13, no. 4, p. 101636, 2022.

[55] Ansys Inc., "SMART crack growth and fracture modelling," White Paper, 2021. [Online]. Available: https://www.ansys.com. Accessed: Dec. 2, 2024.

[56] T. Schneider, Y. Hu, X. Gao, J. Dumas, D. Zorin, D. Panozzo, "A large-scale comparison of tetrahedral and hexahedral elements for solving elliptic PDEs with the finite element method," *ACM Transactions on Graphics*, vol. 41, no. 3, pp. 1–14, 2022.

[57] Ansys Inc., *ANSYS Mechanical User's Guide*, Release 2024 R1, Canonsburg, PA, USA, 2024.

[58] Ansys Inc., "ANSYS Help: Fracture analysis," 2024. [Online]. Available: https://ansyshelp.ansys.com. Accessed: Dec. 1, 2025.

[59] A. M. Alshoaibi, Y. A. Fageehi, "Comparative analysis of 3D software for fatigue crack growth," *Applied Sciences*, vol. 14, no. 5, p. 1848, 2024.

[60] H. Radhakrishnan, J. Manuel, "Fatigue crack growth in pipe fittings," in *Proc. ASME PVP Conf.*, Atlanta, GA, USA, 2023.

[61] N. Moës, J. Dolbow, T. Belytschko, "A finite element method for crack growth without remeshing," *International Journal for Numerical Methods in Engineering*, vol. 46, no. 1, pp. 131–150, 1999.

[62] A. A. Sipos, S. Cao, "Measuring stress intensity factors in curved brittle shells," *Frattura ed Integrità Strutturale*, vol. 18, no. 69, pp. 1–17, 2024.

[63] MatWeb, "Aluminium 7075-T6; 7075-T651," Material Data Sheet. [Online]. Available: https://www.matweb.com. Accessed: Dec. 1, 2025.

[64] M. Dallago, S. Raghavendra, V. Luchin, G. Zappini, D. Pasini, M. Benedetti, "The role of node fillet, unit-cell size and strut orientation on the fatigue strength of Ti-6Al-4V lattice materials additively manufactured via laser powder bed fusion," *International Journal of Fatigue*, vol. 142, p. 105946, 2020.

[65] M. Aursand, B. H. Skallerud, "Mode I stress intensity factors for semi-elliptical cracks," *Theoretical and Applied Fracture Mechanics*, vol. 112, p. 102904, 2021.

[66] S. Ataya, N. H. Alrasheedi, M. M. El-Sayed Seleman, R. G. Eid, A. Bakkar, A. Ataya, et al., "RSM-based optimisation of AZ91 composites," *Processes*, vol. 13, no. 6, p. 1697, 2025.

[67] R. Jones, C. Rans, A. P. Iliopoulos, J. G. Michopoulos, N. Phan, D. Peng, "Crack growth variability in SLM Ti-6Al-4V," *Materials*, vol. 14, no. 6, p. 1400, 2021.

[68] J. Toribio, B. González, J.-C. Matos, I. González, "Notch effects on stress intensity factors," *Materials*, vol. 15, no. 24, p. 9091, 2022.

[69] G. Glinka, W. Ott, H. Nowack, "Elastoplastic plane strain analysis at notch roots," *Journal of Engineering Materials and Technology*, vol. 110, no. 3, pp. 195–204, 1988.

[70] F. E. Harrell, *Regression Modeling Strategies*. Cham, Switzerland: Springer, 2015.

[71] M. Riani, A. C. Atkinson, A. Corbellini, "Robust Box–Cox and Yeo–Johnson transformations," *Statistical Methods and Applications*, vol. 32, pp. 75–102, 2022.

[72] A. Garcia-Gonzalez, J. A. Aguilera, P. M. Cerezo, C. Castro-Egler, P. Lopez-Crespo, "Crack tip plasticity in fatigue crack growth models," *Materials*, vol. 16, no. 24, p. 7603, 2023.

[73] A. Zangeneh, I. Sattarifar, M. Noghabi, "Residual stress effects on fatigue crack propagation," *Journal of Mechanical Engineering and Sciences*, vol. 16, no. 2, pp. 9187–9196, 2022.

[74] M. Opazo Breton, D. Gillespie, R. Pryce, I. Bogdanovica, C. Angus, M. Hernandez Alava, et al., "Long-term smoking trends using APC models," *Addiction*, vol. 117, no. 5, 2021.

[75] M. Afrazi, Q. Lin, A. Fakhimi, "Mode II fracture of quasi-brittle materials," *International Journal of Civil Engineering*, vol. 20, no. 9, pp. 993–1007, 2022.

[76] S. R. Vempati, K. Brahma Raju, K. Venkata Subbaiah, "Simulation of Ti-6Al-4V cruciform welded joints subjected to fatigue load using XFEM," *Journal of Mechanical Engineering and Sciences*, vol. 13, no. 3, pp. 5371–5389, 2019.

[77] O. C. Şen, R. Janisch, "Crack configuration influence on fracture behaviour," *Modelling and Simulation in Materials Science and Engineering*, vol. 32, no. 6, p. 065033, 2024.

[78] C. Ding, R. Yang, C. Xiao, Y. Zhao, Y. Wang, C. Chen, "Influence of the notch curvature on the impact fracture of the three-point bending beam," *Engineering Fracture Mechanics*, vol. 241, p. 107419, 2021.